Materials Advances

ROYAL SOCIETY OF CHEMISTRY

PAPER

View Article Online
View Journal | View Issue

Cite this: *Mater. Adv.*, 2025, **6**, 5506

Insights into structural, luminescence and temperature-dependent emission characteristics of $Ca_2Al_2O_5:Dy^{3+}$ phosphors for advanced lighting applications†

A. Vidya Saraswathi,[a] Tejas,[a] S. Masilla Moses Kennedy,[b] A. Princy,[b] M. I. Sayyed,[cd] Aljawhara H. Almuqrin,[e] Vikash Mishra[a] and Sudha D. Kamath *[a]

Received 23rd April 2025,
Accepted 19th June 2025

DOI: 10.1039/d5ma00391a

rsc.li/materials-advances

This research synthesized and thoroughly examined novel $Ca_2Al_2O_5:Dy^{3+}$ phosphors to assess their potential for solid-state lighting and temperature-sensing applications. X-ray diffraction (XRD) verified the formation of a cubic phase with Dy^{3+} ions successfully integrated into the $Ca_2Al_2O_5$ host lattice. Photoluminescence (PL) analysis showed distinct blue (483 nm), yellow (575 nm), and weak red (663 nm) emissions, corresponding to the $^4F_{9/2} \rightarrow {}^6H_{15/2}$, $^4F_{9/2} \rightarrow {}^6H_{13/2}$, and $^4F_{9/2} \rightarrow {}^6H_{11/2}$ transitions of Dy^{3+}, respectively. The study identified that a 2 mol% concentration of Dy^{3+} is the ideal doping to achieve optimal luminescence, and the emission falls in the cool white light region. The optical study was used to ascertain the optical band gap, and the band gap of the host matrix decreases upon doping (from 5.01 eV to 4.83 eV) as new defect energy levels appear between the valence band and the conduction band. Temperature-dependent photoluminescence (TDPL) studies demonstrated excellent thermal stability, with the phosphors retaining significant luminescence intensity even at elevated temperatures. These phosphors exhibit appreciable thermal quenching behaviour and possess an activation energy of 0.20051 eV, underscoring their resilience at high temperatures. These results highlight the promising optical performance and thermal durability of $Ca_2Al_2O_5:Dy^{3+}$ phosphors, making them strong candidates for white LEDs and temperature-sensitive optoelectronic devices.

1. Introduction

Phosphor materials are vital in advancing light-emitting technologies, acting as a key element in fields such as solid-state lighting, display systems, and radiation detection. When activated by different energy sources, including ultraviolet light, heat, or electrical fields, these substances exhibit luminescence, effectively converting energy into visible light. Their high quantum efficiency and customizable emission characteristics make them indispensable in devices like light-emitting diodes (LEDs), fluorescent lamps, and electroluminescent displays. With the increasing demand for energy-efficient lighting solutions, developing high-performance phosphors with robust thermal stability and strong emission intensity has become a primary focus in materials research.[1,2]

The properties of a phosphor, including its emission wavelength, intensity, afterglow, and thermal quenching behaviour, are influenced by the combination of its host lattice and the dopant ions. Numerous host-dopant pairings have been developed to achieve superior emission qualities. For instance, $YAG:Ce^{3+}$ is frequently utilized in white LEDs due to its broad yellow emission, which blends with blue light to create white light.[3,4] Other significant systems include (Sr,Ca)S:Eu for red emission in fluorescent lamps,[5] Zn_2SiO_4:Mn for use in flat panel displays,[6] and $BaMgAl_{10}O_{17}:Eu^{2+}$ for blue emission in LED displays.[7] Long-lasting phosphors like $SrAl_2O_4:Eu^{2+},Dy^{3+}$ are particularly valued for emergency lighting and glow-in-the-dark uses.[8–10] Moreover, phosphors based on nitrides[11–13] and oxynitrides[14–16] are noted for their high quantum efficiency and thermal stability, making them excellent red emitters in LEDs. Similarly, hosts made of silicate,[17–19] borate,[20–22] aluminate,[23,24] vanadate,[25–27] and fluoride[28–30] when doped with rare-earth ions offer a variety of optical properties

[a] Department of Physics, Manipal Institute of Technology, Manipal Academy of Higher Education, Manipal 576104, Karnataka, India. E-mail: sudha.kamath@manipal.edu
[b] Sri Siva Subramaniya Nadar College of Engineering, Tamilnadu, India
[c] Renewable Energy and Environmental Technology Center, University of Tabuk, Tabuk, 47913, Saudi Arabia
[d] Department of Physics and Technical Sciences, Western Caspian University, Baku, Azerbaijan
[e] Department of Physics, College of Science, Princess Nourah bint Abdulrahman University, P.O. Box 84428, Riyadh 11671, Saudi Arabia

† Electronic supplementary information (ESI) available. CCDC. For ESI and crystallographic data in CIF or other electronic format see DOI: https://doi.org/10.1039/d5ma00391a

suitable for lasers,[31,32] displays,[33–35] bioimaging,[36,37] and up-conversion applications.[38–40]

Among these, aluminate-based phosphors have gained considerable attention due to their excellent chemical stability, long afterglow, and suitability for high-temperature applications.[41,42] There are reports on structural and luminescence properties of $Sr_4Al_{14}O_{25}$:Eu/Dy,[41] electronic structure and high-pressure luminescence studies of $Sr_4Al_{14}O_{25}$:Mn,[42] JO analysis of $LaAlO_3$:Tm,[43] luminescence of $LaAlO_3$:Eu,[44] computational and spectroscopic study of Eu/Nd doped MAl_2O_4 (M = Ca, Sr, Ba), radioluminescence of $SrAl_2O_4$:Eu,Sm,Dy,[45] emission studies of $SrAl_2O_4$:Er,[46] Eu/Dy,[47,48] $CaAl_2O_4$:Eu/Nd,[49] Pr,[50] Sm,[51] thermoluminescence characteristics of $CaAl_2O_4$:Dy,Sm,Tm,[52] trap depth analysis of $CaAl_2O_4$:Tb,[53] $LaMgAl_{11}O_{19}$:Eu,[54] temperature dependent luminescence studies of $BaMgAl_{10}O_{17}$:Ce,Tb,[55] luminescence features of $BaMgAl_{10}O_{17}$:Eu,[56–58] Cr,[59] $BaMgAl_{10}O_{17}$:Mn,[60] $BaMgAl_{10}O_{17}$:Eu,Yb,[61] $BaMgAl_{10}O_{17}$:Dy,[62] $SrMgAl_{10}O_{17}$:Eu,Dy,[63] $SrMgAl_{10}O_{17}$:Mn,Eu,[64] $Ca_2Al_2O_5$:Eu,[65,66] and mechanoluminescence studies of $SrMgAl_{10}O_{17}$:Eu[67] phosphors.

After thoroughly reviewing the literature, we selected $Ca_2Al_2O_5$ as the host matrix and Dy^{3+} as the dopant. $Ca_2Al_2O_5$ phosphors are renowned for their outstanding thermal and chemical stability, even in high-temperature and challenging environmental conditions. This characteristic makes them ideal for applications involving high-power or high-temperature lighting. The $Ca_2Al_2O_5$ system can be produced through a cost-effective solid-state method using readily available raw materials ($CaCO_3$ and Al_2O_3). In contrast to well-known hosts like $SrAl_2O_4$ or YAG, $Ca_2Al_2O_5$ has not been extensively studied, especially in Dy^{3+} doping. To our knowledge, only one prior study has explored Dy^{3+} in this host, and it did not provide a comprehensive analysis of structural, luminescence, and temperature-dependent emission properties. Since the studies are limited to $Ca_2Al_2O_5$:Dy, the present work focuses on the structural, morphological, and luminescence properties along with in-depth analysis of crystallite size, correlation between dopant concentration and luminescence features. Furthermore, the temperature-dependent luminescence characteristics are explored with critical insights into activation energy and FWHM variation. Thermal stability and activation energy contribute to designing and optimizing tools for elevated temperature applications such as solid-state lighting and display applications.

2. Experimental details

2.1 Sample synthesis

The $Ca_2Al_2O_5$:Dy (CAO–Dy) phosphors were prepared by varying the amount of Dy^{3+} from 1 mol% to 5 mol%. The precursors $CaCO_3$, Al_2O_3, and Dy_2O_3 were taken in stoichiometric ratios and mixed well in a mortar for 45 minutes. To ensure homogenous mixing, we added ethanol while grinding the sample. The mixture was calcined at 1300 °C for 8 hours at a heating rate of 5 °C min^{-1}. The samples were collected after attaining room temperature for further characterization.

2.2 Characterization techniques

The structural studies are conducted using a Rigaku Miniflex 600 (5th generation) device, which employs K-α radiation (λ = 1.54 Å), voltage maintained at 40 kV and current at 15 mA. A SHIMADZU-IRSpirit ATR-FTIR spectrometer is utilized to identify functional groups. The morphology of the samples is analyzed with SEM technique using a Sigma Zeiss instrument. Diffuse reflectance data is gathered with a PerkinElmer Lambda 900 spectrophotometer. The emission characteristics are recorded utilizing a JASCO-FP 8500. The variation in luminescence properties with temperature is obtained with an Agilent Cary Eclipse Fluorescence Spectrophotometer.

3. Results and discussion

3.1 X-ray diffraction (XRD) study

The synthesized samples' phase confirmation and crystal structure are obtained by XRD analysis. Fig. 1(a) shows the XRD peaks of CAO–Dy samples, which match the COD code – 1525613 pattern. There is no appreciable peak shift with changing dopant concentration, and the crystal structure remains unaltered upon doping. Fig. 1(b) shows the crystal structure of the CAO unit cell. The Rietveld refinement was performed to ascertain the lattice parameters, volume, and phase purity (Fig. 1(c)). This analysis indicated the formation of a cubic lattice with space group $I\bar{4}3d$, crystal parameters $a = b = c$ = 11.9953 Å, and $\alpha = \beta = \gamma = 90°$, and the volume is 1725.97 $Å^3$. No impurity peaks were observed in the XRD pattern. The reliability factors obtained are R_p: 32% and R_{wp}: 33%, with structural coordinates and occupation detailed in Table 1. As depicted in Fig. 2(b), the refinement data shows an excellent fit with χ^2 = 2.74.

To explore the dopant's occupation site, we must focus on the dopant ion's ionic radii and the cation being replaced in the host matrix.[68] For each cation and dopant pair for a different coordination number (CN), the acceptable percentage difference value (R) is calculated as per the following equation.

$$R = \frac{|R_h(\mathrm{CN}) - R_d(\mathrm{CN})|}{R_h(\mathrm{CN})} \times 100\% \quad (1)$$

where R_h is the host cation radius, CN is the coordination number, and R_d is the radius of the dopant ion. If R is well below 30%, the substitution of dopant to the respective cationic site is confirmed. The calculation for the R-value is given in the Table 2. From Table 2, R < 30% for Ca^{2+}–Dy^{3+} combination; hence we can confirm the occupation of dopant ion in Ca^{2+} sites.[69,70] The crystallite size of CAO–Dy samples is calculated using the Debye–Scherrer equation and size-strain plot (SSP) approach. The crystallite size affects the diffraction pattern and the luminescence features of phosphors. The crystallite size varies with dopant concentration and is calculated using the following Debye–Scherrer equation[71,72]

$$D = \frac{k\lambda}{\beta\cos\theta} \quad (2)$$

λ is the X-ray wavelength (1.54 Å), β is the full-width half maximum of the XRD peak, and k is a constant taken as 0.9. The crystallite size variation is also determined using the SSP method, where the higher angle reflections are given less weight as they have lower precisions. The Lorentzian function

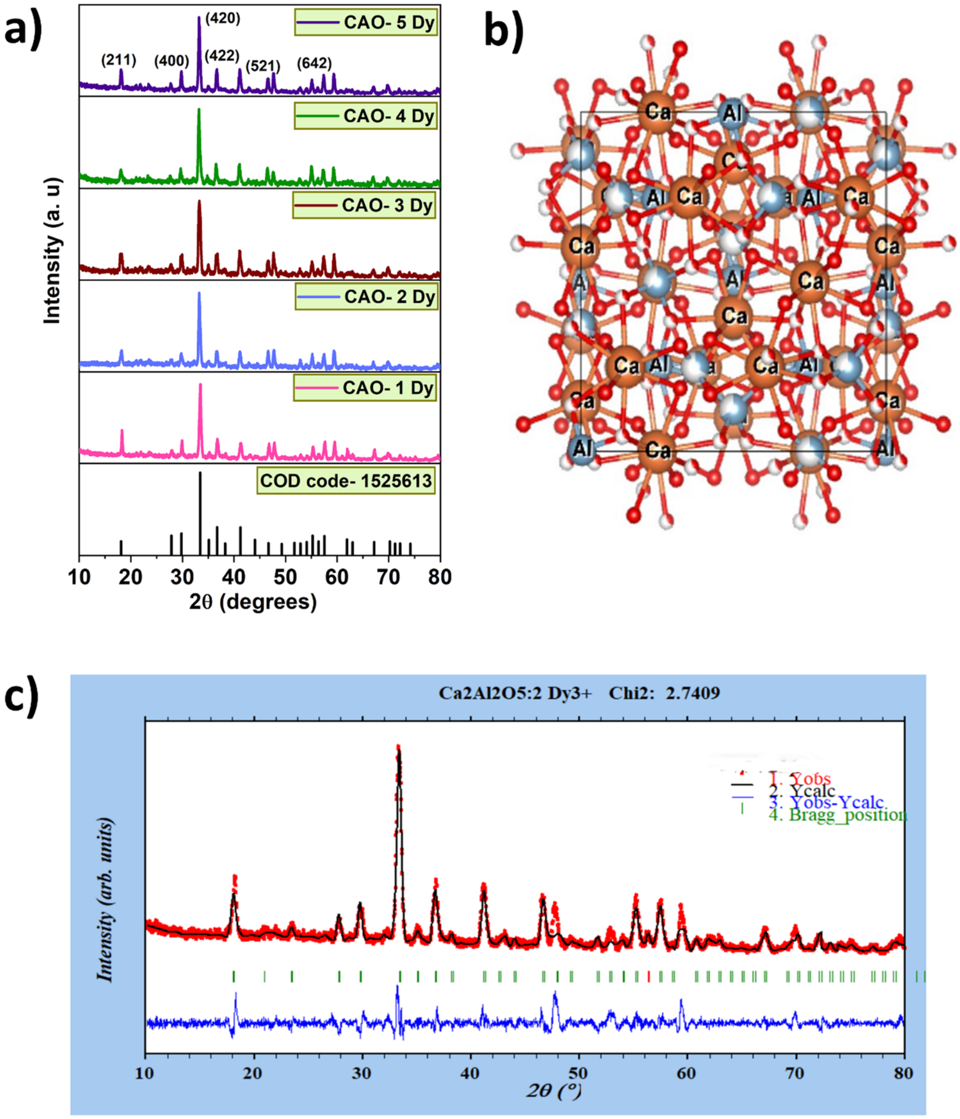

Fig. 1 (a) XRD pattern of CAO phosphor for varying Dy^{3+} concentration, and (b) CAO unit cell, (c) Rietveld refinement of CAO–2 Dy sample.

and Gaussian functions are used to illustrate the crystallite size profile and the strain profile, respectively, as per the following equation,[73,74]

$$(d_{hkl}\beta_{hkl}\cos\theta)^2 = \frac{K}{D}(d_{hkl}{}^2\beta_{hkl}\cos\theta) + \left(\frac{\varepsilon}{2}\right)^2 \tag{3}$$

where K is 0.75, which depends on the shape of the particles, ε is the strain, d_{hkl} is the interplanar spacing. By taking the slope (K/D) of $(d_{hkl}\beta_{hkl}\cos\theta)^2$ *vs.* $(d_{hkl}{}^2\beta_{hkl}\cos\theta)$ graph, the crystallite size can be calculated (Fig. 2). Table 3 gives the variation in crystallite size of CAO–Dy phosphors calculated using Debye–Sherrer and SSP methods.

The average crystallite size of CAO–Dy samples was 18–23 nm using Scherrer's method and 66–75 nm range for the SSP method. This difference might be attributed to the inclusion of strain in the latter method.

3.2 Fourier transform infrared (FTIR) spectroscopy

The vibrational functional groups of phosphor samples are identified using FTIR spectroscopy. Fig. 3 shows the vibrational bands in the CAO host matrix and Dy^{3+} doped CAO. Region 1 (in Fig. 3) displays bands at 745 cm^{-1} and 806 cm^{-1}, corresponding to Ca–O vibrations.[75] The same bands appear in the Dy^{3+} doped sample as well. As the dopant occupies Ca^{2+} sites, there is no peak shift (shift is within error limit) or band appearance/disappearance upon Dy^{3+} doping, confirming the unaltered structure of the host matrix upon doping. The regions identified as 2 and 3 (Fig. 3) are assigned to Al–O vibrations, having bands at 514 and 571 cm^{-1}.[76]

3.3 Scanning electron microscopy (SEM)

The morphological features of CAO–Dy samples are shown in the Fig. 4. Highly agglomerated microstructure accompanied by porous morphology is obtained for the prepared sample.[77] The

Table 1 Sample notation

Chemical formula	Notation
$Ca_2Al_2O_5$:1 mol% Dy	CAO–1 Dy
$Ca_2Al_2O_5$:2 mol% Dy	CAO–2 Dy
$Ca_2Al_2O_5$:3 mol% Dy	CAO–3 Dy
$Ca_2Al_2O_5$:4 mol% Dy	CAO–4 Dy
$Ca_2Al_2O_5$:5 mol% Dy	CAO–5 Dy

shape of the particles is irregular, and accurate particle measurement is impossible.[78]

3.4 Optical studies

Fig. 5(a) gives the Diffuse reflectance (DR) spectra of CAO–2 Dy phosphor, the peaks are centred at 490 nm, 792 nm, 880 nm, 1060 nm, 1252 nm, 1380 nm, and 1650 nm attributed to transitions $^6H_{15/2} \rightarrow {}^4F_{9/2}$, $^6H_{15/2} \rightarrow {}^6F_{5/2}$, $^6H_{15/2} \rightarrow {}^6F_{7/2}$, $^6H_{15/2} \rightarrow {}^6H_{7/2}$, $^6H_{15/2} \rightarrow {}^6F_{11/2}$, $^6H_{15/2} \rightarrow {}^6H_{9/2}$, and $^6H_{15/2} \rightarrow {}^6H_{11/2}$ respectively. These transitions are further used to identify the nature of bonding between the dopant ion and the host matrix ligand. The nephelauxetic ratio (β) and bonding parameter (δ) are given using the following equations[79]

$$\beta = \frac{\nu_c}{\nu_a} \tag{4}$$

N_c and ν_a are the energies of the Dy^{3+} transitions in the host matrix and the aqueous solutions, respectively.[80]

$$\delta = \frac{1-\beta_{avg}}{\beta_{avg}} \tag{5}$$

where β_{avg} is the average value of β for observed transitions, if $\delta < 0$, the bonding is ionic, and $\delta > 0$ corresponds to covalent bonding. Table 4 gives the values of β and δ for the Dy^{3+} transitions.

Since the δ value is 0.00623, the Dy^{3+}–ligand bond is covalent for the prepared phosphor samples. A similar covalent

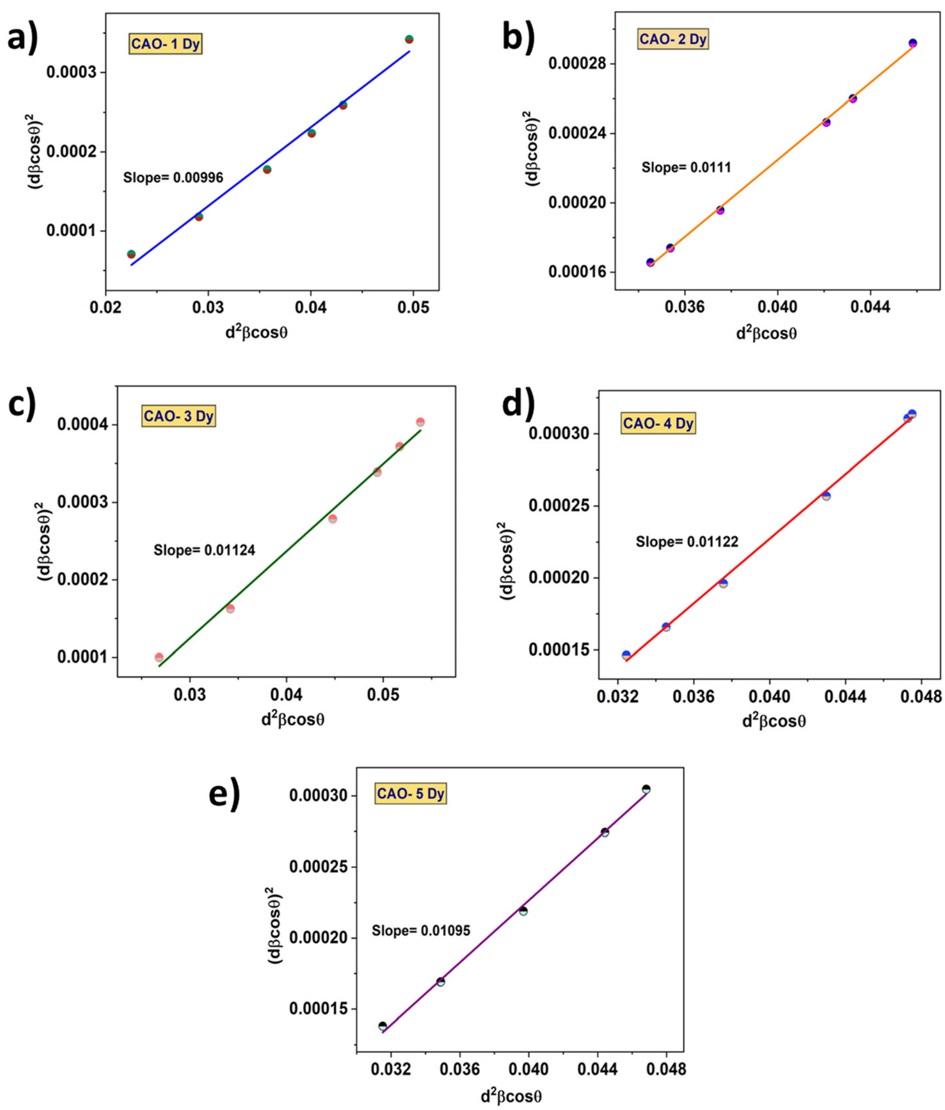

Fig. 2 (a)–(e) Crystallite analysis using the SSP method for CAO–Dy samples.

Table 2 R values for different cation-dopant combinations

Ca^{2+}–Dy^{3+} pair				
CN of Ca^{2+}	R_h (CN)	CN of Dy^{3+}	R_d (CN)	R (%)
6	1	6	0.912	8.8
6	1	8	1.027	2.7
8	1.12	6	0.912	18.57
8	1.12	8	1.027	20.30
Al^{3+}–Dy^{3+} pair				
CN of Al^{3+}	R_h (CN)	CN of Dy^{3+}	R_d (CN)	R (%)
6	0.535	6	0.912	70.40
6	0.535	8	1.027	91.90

Table 3 Crystallite size variation using Scherrer's formula and SSP approach

Sample name	2θ (degrees)	FWHM (degrees)	Scherrer's method D (nm)	SSP method D (nm)
CAO–1 Dy	33.415	0.4124	20.10	75.30
CAO–2 Dy	33.2474	0.4477	18.50	68.20
CAO–3 Dy	33.2023	0.3594	23.05	66.72
CAO–4 Dy	33.2158	0.3692	22.44	66.85
CAO–5 Dy	33.1194	0.3928	21.10	68.50

nature of dopant-ligand covalent band is reported in previous studies.[81–83]

The optical energy band gap of pure and optimized CAO–2 Dy samples is calculated using Tauc plot, using the following equation,[84,85]

$$[F(R)\cdot E]^{\frac{1}{n}} = K(E - E_g) \tag{6}$$

$$F(R) = \frac{(1-R)^2}{2R} \tag{7}$$

where $F(R)$ is the Kubelka Munk function, E_g is the energy band gap of the material, E is the energy of incident radiation, and R is the sample's reflectance. The value of n differs based on the type of bandgap observed. For direct band gap, $n = 0.5$ and for indirect bandgap, $n = 2$. For the synthesized CAO and CAO–2 Dy samples, the best fit is observed for $n = 0.5$, and the x-intercept of $(F(R)h\nu)^2$ *vs.* photon energy plot gives the energy gap (Fig. 5(b)). The band gap of pure CAO is 5.01 eV; upon doping, the band gap decreases to 4.83 eV. This bandgap reduction is attributed to forming defect states between the forbidden gap by adding Dy^{3+} ions. Such a decreasing trend in the energy gap is observed and reported in the literature.[86–88]

3.5 Photoluminescence (PL) analysis

The luminescence properties of Dy-doped CAO phosphors are crucial for understanding their potential applications in solid-state lighting. The excitation spectrum of Dy-doped CAO samples is recorded for a fixed emission wavelength of 575 nm (given in Fig. 6(a)). There are excitation peaks observed at 295 nm, 325 nm, 351 nm, 387 nm, 426 nm, 454 nm, and 465 nm corresponding to the transitions $^6H_{15/2} \rightarrow {}^4D_{7/2}$, $^6H_{15/2} \rightarrow {}^6P_{3/2}$, $^6H_{15/2} \rightarrow {}^6P_{7/2}$, $^6H_{15/2} \rightarrow {}^4M_{21/2}$, $^6H_{15/2} \rightarrow {}^4G_{11/2}$, $^6H_{15/2} \rightarrow {}^4I_{15/2}$ and $^6H_{15/2} \rightarrow {}^4F_{9/2}$ respectively.[89,90] The 351 nm peak corresponding to $^6H_{15/2} \rightarrow {}^6P_{7/2}$ is the excitation wavelength to record the emission spectra (Fig. 6(b)). Dy^{3+} characteristic emission peaks are obtained at 483 nm ($^4F_{9/2} \rightarrow {}^6H_{15/2}$), 575 nm ($^4F_{9/2} \rightarrow {}^6H_{13/2}$), and 663 nm ($^4F_{9/2} \rightarrow {}^6H_{11/2}$).[91] The emission intensity shows an increasing trend with Dy^{3+} concentration up to 2 mol%, beyond which the PL intensity reduces (Fig. 6(c)). The reason for the variation in PL intensity is correlated with dopant concentration, which is called concentration quenching. The quenching in PL intensity can be explained using cross-relaxation (CR) paths between neighbouring Dy^{3+} ions. Fig. 7 illustrates the energy level diagram and the potential cross-relaxation pathways for the Dy^{3+} ions.[92] In this context, we identify three distinct energy transfer (ET) channels between identical Dy^{3+} ions within the CAO host, designated CR1, CR2, and CR3. The ET channels result in non-radiative energy transfer; hence, the emission intensity decreases. The ET transitions are given below.[93,94]

$$\text{CR1: } {}^4F_{9/2} \rightarrow {}^6F_{9/2} + {}^6H_{7/2} \approx {}^6H_{15/2} \rightarrow {}^6F_{5/2}$$

$$\text{CR2: } {}^4F_{9/2} \rightarrow {}^6F_{11/2} + {}^6H_{9/2} \approx {}^6H_{15/2} \rightarrow {}^6F_{3/2}$$

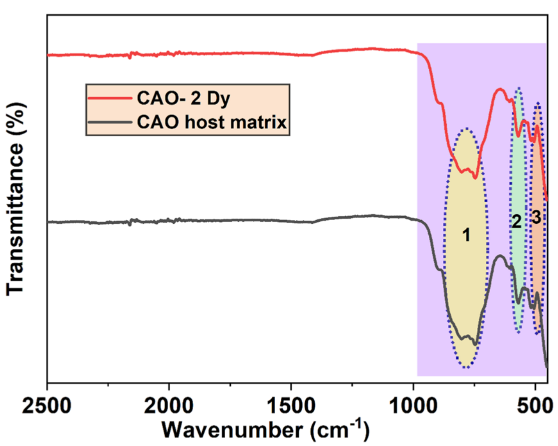

Fig. 3 FTIR spectra of CAO host and CAO–2 Dy samples.

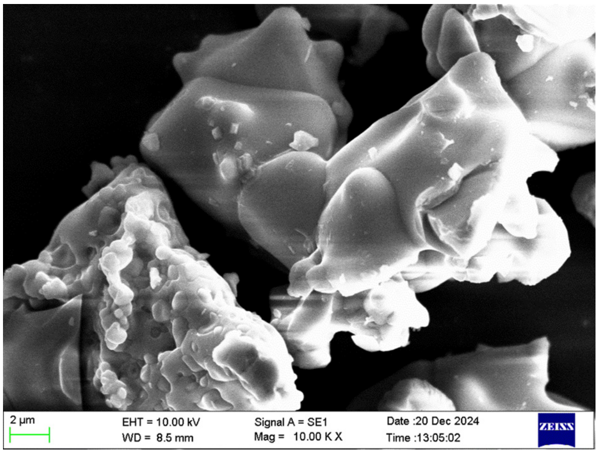

Fig. 4 Surface morphology of CAO–2 Dy phosphor.

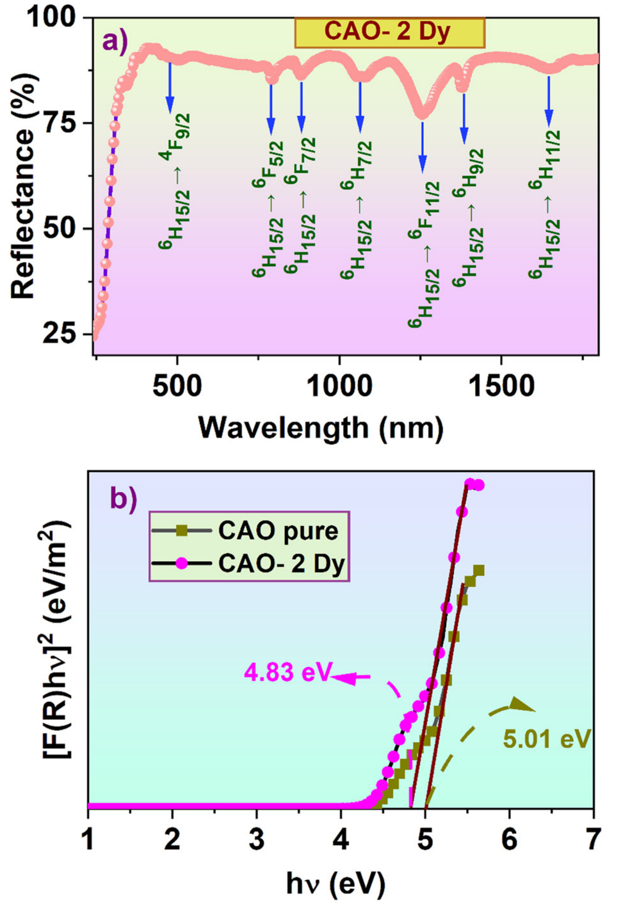

Fig. 5 (a) DR spectrum of CAO–2 Dy phosphor, (b) optical band gap of pure and doped CAO samples.

$$\text{CR3: } {}^4F_{9/2} \rightarrow {}^6F_{3/2} \approx {}^6H_{15/2} \rightarrow {}^6F_{11/2} + {}^6H_{9/2}$$

In addition to the cross-relaxation mechanism, the ET can be associated with the multipolar or exchange interactions among Dy^{3+} ions. The mode of ET is determined by estimating the critical radius R_c using the below equation,

$$R_c = 2\left(\frac{3V}{4\pi X_c N}\right)^{1/3} \tag{8}$$

where the unit cell volume, V = 1725.97 Å^3, optimum concentration; X_c = 0.02, and N = 2. The value of R_c = 43.517 Å. As the critical distance exceeds 5 Å, indicating that concentration quenching results from multipolar interaction. Several multipolar interactions exist, including dipole–dipole, dipole–quadrupole, and quadrupole–quadrupole. Dexter's theory[95] can be employed to determine the specific multipolar interaction in CAO–Dy phosphors (eqn (9)).

$$\log\frac{I}{x} = c - \frac{\theta}{3}\log x \tag{9}$$

The relationship between $\log I/x$ and $\log x$ exhibit a slope of $-(\theta/3)$, where θ serves as an indicator of the multipolar interaction type (Fig. 8(a)). Specifically, θ values of 6, 8, and 10 correspond to dipole–dipole, dipole–quadrupole, and quadrupole–quadrupole reactions. An analysis of the graph depicting log(I/x) against log(x) reveals a slope of −1.73537. Given that $\theta \approx 5.20$ approximates 6, the data suggests that dipole–dipole interactions predominantly govern the energy transfer mechanism.[96,97] The reduction in PL intensity could be related to substituting the Dy^{3+} ion into the Ca^{2+} site. The charge imbalance leads to the formation of defects. The probable defects introduced to maintain charge neutrality are oxygen vacancies (Vo) and cationic vacancies (V_{Ca}). These defects act as electron traps, reducing the emission intensity.[98,99]

The intense yellow emission ($^4F_{9/2} \rightarrow {}^6H_{13/2}$) due to electric dipole is more intense than the magnetic dipole transition corresponding to the blue emission ($^4F_{9/2} \rightarrow {}^6H_{15/2}$). Thus, we can specify that the Dy^{3+} ions do not occupy inversion symmetry sites as the hyper-sensitive electric dipole transition is dominant (Fig. 8(b)). The magnetic dipole transition will be predominant if the dopant ions occupy inversion symmetry sites.[100] The Y/B ratios for CAO–Dy samples are 2.15, 2.24, 2.32, 2.37, and 2.32 for 1, 2, 3, 4, and 5 mol% of dopant concentration (Fig. 8(c)). As the $(Y/B) > 1$, the emission appears to be yellowish-white light rather than pure white light.[101,102]

Table 4 Bonding parameter calculation for CAO–2 Dy

Sl. number	Transition from $^6H_{15/2}$ to	ν_c (cm^{-1})	ν_a (cm^{-1})	β
1	$^4F_{9/2}$	20 963	21 100	0.9935
2	$^6F_{5/2}$	12 323	12 400	0.9938
3	$^6F_{7/2}$	10 926	11 000	0.9932
4	$^6H_{7/2}$	9014	9100	0.9905
5	$^6F_{11/2}$	7667	7700	0.9957
6	$^6H_{9/2}$	7637	7692	0.9928
7	$^6H_{11/2}$	5835	5850	0.9974
$\boldsymbol{\beta_{avg}}$				**0.9938**

3.6 Photometric analysis

The tristimulus values determine the colour coordinates of the prepared phosphor sample (refer to eqn (S1)–(S6), ESI†),[103]

In the Fig. 9, the colour coordinates fall in the yellowish-white region, and the colour purity is estimated using the below formula[104]

$$\text{Colour purity (CP)} = \frac{\sqrt{(x_s - x_0)^2 + (y_s - y_0)^2}}{\sqrt{(x_d - x_0)^2 + (y_d - y_0)^2}} \tag{10}$$

The coordinates (x_0, y_0), (x_s, y_s), and (x_d, y_d) represent the epicentre of convergence (0.332, 0.186), coordinates of the phosphor sample, and coordinates of the dominant emission, respectively. The correlated colour temperature is determined using McCamy's formula[105]

$$\text{CCT} = -449n^3 + 3525n^2 - 6823n + 5520.33 \tag{11}$$

where n is the slope of the inverse line, $n = (x - x_0)/(y - y_0)$.

The colour rendering index (CRI) measures how accurately a light source displays colours by comparing it to an ideal or natural lighting benchmark. The quality of light source is evaluated depending on the range of CRI value. The CRI range is 68–72, corresponding to a good light source with high accuracy in colour appearance.

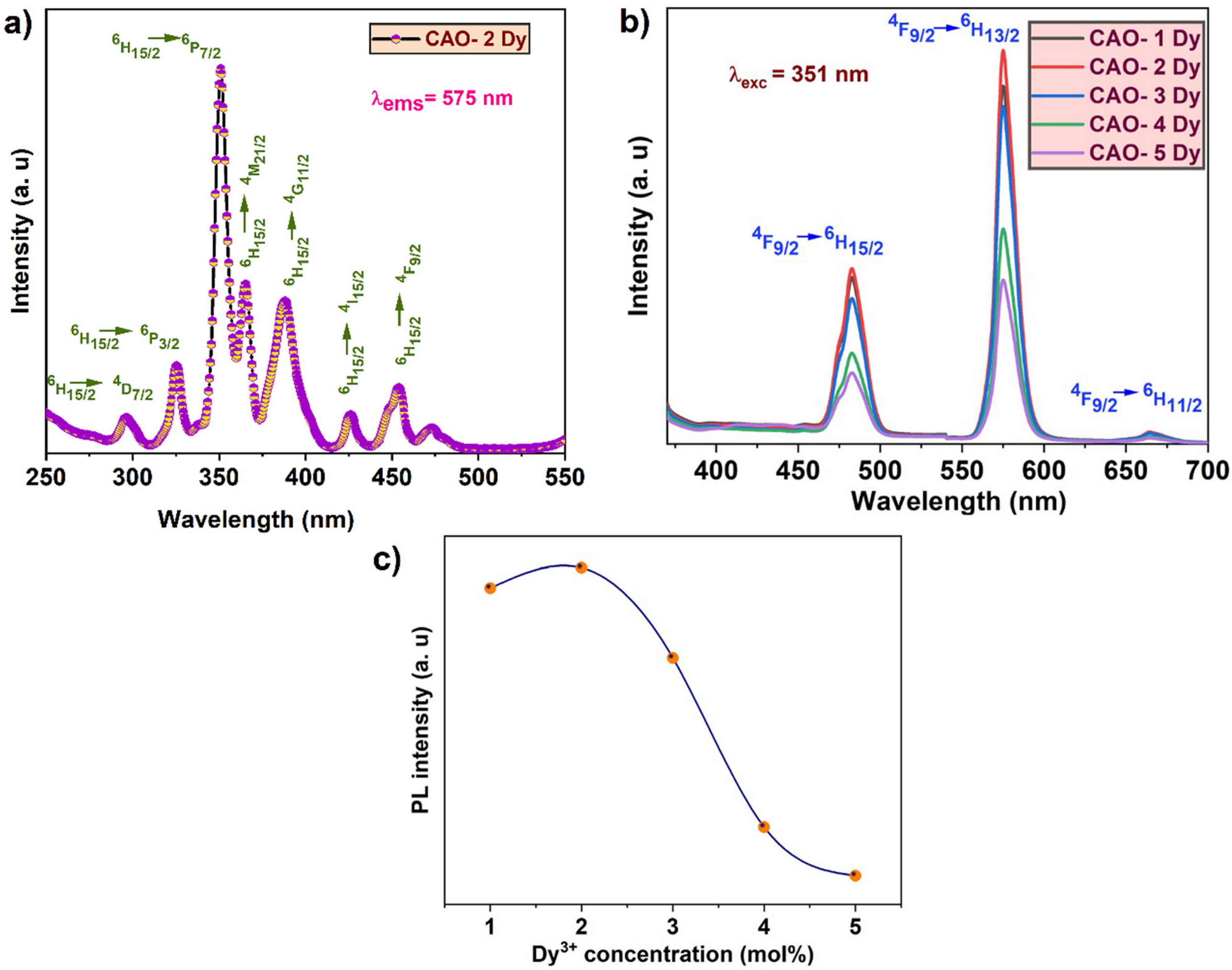

Fig. 6 (a) Excitation spectrum of CAO–2 Dy phosphor, (b) emission spectra of CAO samples for different dopant concentrations, and (c) variation in PL intensity as a function of Dy^{3+} concentration.

Table 5 gives the colour coordinates, colour purity, and CRI and CCT values of CAO–Dy phosphors. Table 6 compares emission wavelength, Colour coordinates, CCT, CP, and CRI values of other phosphors and the present work. The synthesized CAO–Dy phosphors emit cool white light (CCT > 4000 K) with good CRI value; hence, they have potential cool/neutral light generation applications.

3.7 Lifetime analysis

Monitoring the excitation wavelength at 351 nm and the emission wavelength at 575 nm allowed the determination of the luminescence lifetime of the $Ca_2Al_2O_5{:}xDy^{3+}$ [x = 1, 2, 3, 4, and 5 mol%] phosphors. Fig. 10(a) displays the decay profile, which displays the intensity as a function of decay lifetime. A single exponential decay function fit was used to further examine the experimental data, and equation was represented as follows,[116,117]

$$I(t) = Ae^{-\frac{t}{\tau}} + I_0 \tag{12}$$

Here τ is the component of the decay lifetimes, A is the fitting parameter and I_0 the initial fluorescence intensity. The single exponential fit is done and shown in Fig. 10(b).

The prepared $Ca_2Al_2O_5{:}xDy^{3+}$ [x = 1, 2, 3, 4, and 5 mol%] phosphor samples had calculated average lifetimes of 0.8722 ms, 0.9925 ms, 0.9276 ms, 0.8928 ms, and 0.8827 ms respectively. The average lifetime increases for 2 mol% and gradually decreases as the doping concentration rises, indicating that the energy transfer activities between Dy^{3+} ions. Auzel's hypothetical model[118,119] was used to assess this trend, and Fig. 10(c) shows the fitted profile.

$$\tau_c = \frac{\tau_0}{\left(1 + \frac{c}{c_0}\right)e^{-N/3}} \tag{13}$$

In this relation, τ_c is the lifetime at doping concentration c, c_0 is the critical concentration, and N is the number of phonons generated. 1.073 ms is the intrinsic radiative lifetime (τ_0). The following formula may be used to determine the non-radiative relaxation rate (k_{nr}) given the radiative lifespan (τ_0) and the

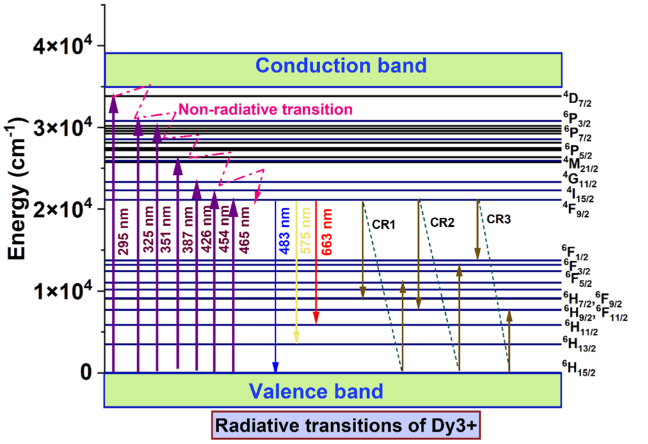

Fig. 7 Energy level diagram of Dy^{3+} ion showing radiative transitions and cross-relaxation paths.

empirically obtained average lifetime (τ_{avg}).[120]

$$\frac{1}{\tau_c} = \frac{1}{\tau_0} + k_{nr} \tag{14}$$

One important metric for evaluating the optical performance of rare earth doped phosphors is quantum efficiency. It may be quantitatively stated in terms of radiative and non-radiative transition rates, as well as the excited-state lifespan, and is defined as the ratio of emitted to absorbed light intensity. The efficiency of energy conversion in luminous materials is

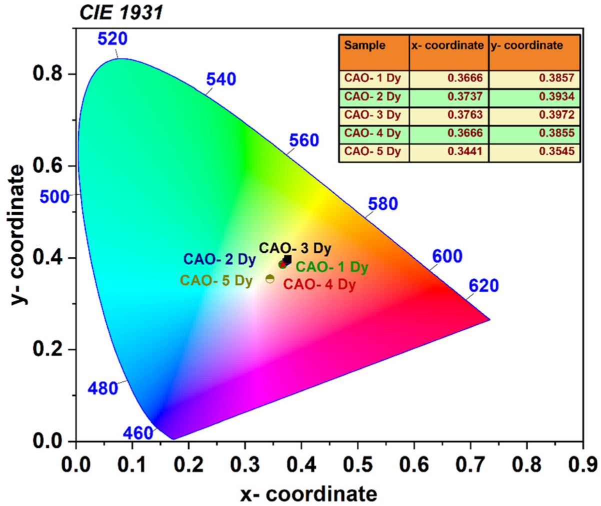

Fig. 9 Chromaticity diagram of CAO–Dy samples.

determined by this metric, which offers a direct measurement of quantum efficiency. The quantum efficiency can be expressed numerically as,[121]

$$\eta = \frac{I_{em}}{I_{ab}} = \frac{k_R}{k_R + k_{nR}} = \frac{\tau_c}{\tau_0} \tag{15}$$

The calculated average lifetime, nonradiative relaxation rate, and quantum efficiency are listed in Table 7.

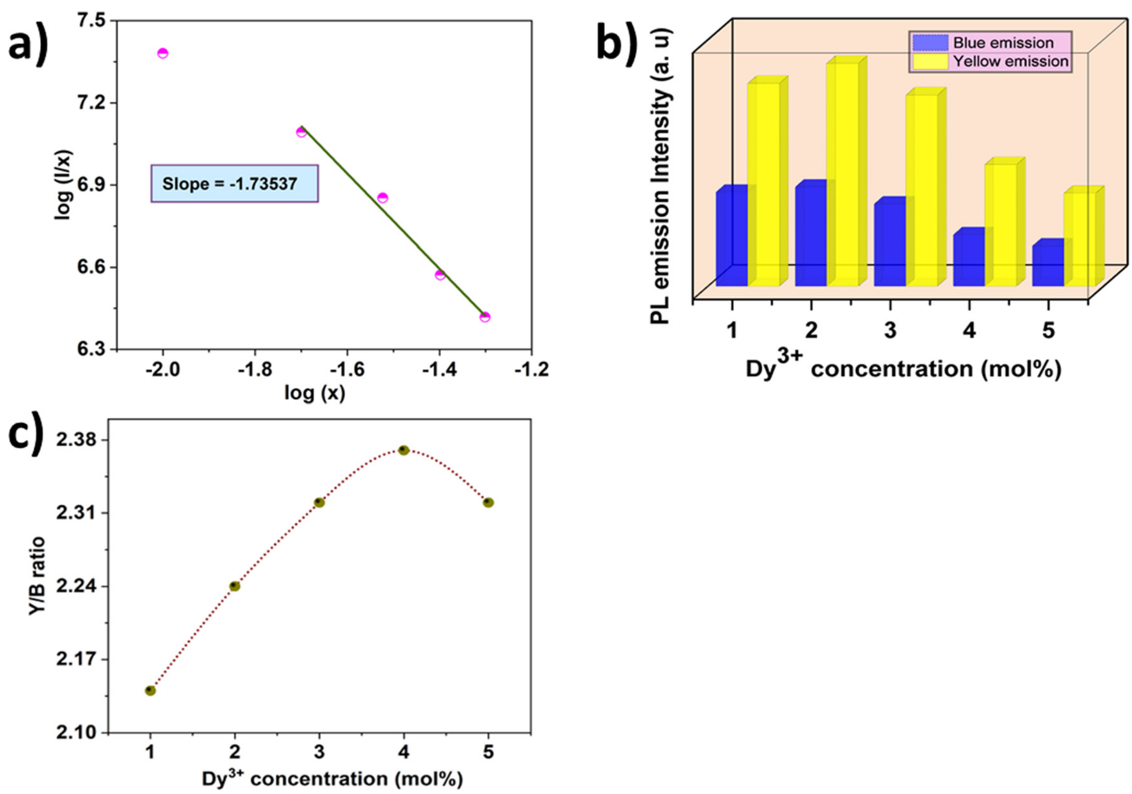

Fig. 8 (a) log(I/x) *versus* log(x) plot for CAO–Dy samples, (b) relative intensity comparison of blue and yellow emission, and (c) Y/B ratio of CAO–Dy phosphors.

Table 5 CIE coordinates and CCT values of CAO–Dy phosphors

Sample code	CIE coordinates (x_s, y_s)	Colour purity (%)	CRI	CCT (K)
CAO–1 Dy	(0.3666, 0.3858)	54	71	4445
CAO–2 Dy	(0.3737, 0.3934)	57	69	4291
CAO–3 Dy	(0.3763, 0.3972)	57	68	4244
CAO–4 Dy	(0.3666, 0.3855)	54	69	4443
CAO–5 Dy	(0.3441, 0.3545)	42	72	5047

3.8 Temperature dependent photoluminescence (TDPL)

Furthermore, the TDPL properties of the optimized CAO–2 Dy were extensively examined to evaluate its thermal stability and emission behaviour at elevated temperatures. The TDPL spectra have the characteristic emission peaks of Dy^{3+} recorded from 303 K to 483 K. A gradual reduction in photoluminescence intensity was observed as the temperature increased (Fig. 11(a)). Thermal quenching is mainly attributed to the increased

Table 6 Comparison of CIE coordinates, colour purity, CRI and CCT values of the optimized phosphor with previously reported works

Phosphor	Emission wavelength (nm)	CIE coordinates (x_s, y_s)	Colour purity (%)	CRI	CCT (K)	Ref.
$Ba_2TeP_2O_9:Dy^{3+}$	573	(0.3981, 0.4333)	55.3	—	3926	106
$CaZn_2(PO_4)_2:Dy^{3+}$	572	(0.3251, 0.3482)	—	80	5815	107
$Y_2CaB_{10}O_{19}:Dy^{3+}$	577	(0.3188, 0.3233)	16.2	77	6209	108
$Y_2O_3:Dy^{3+}$	575	(0.2650, 0.3880)	—	33	8199	109
$GdSr_2AlO_5:Dy^{3+}$	582	(0.3396, 0.3851)	17.6	—	5272	110
$NaSrPO_4:Dy^{3+}$	576	(0.2700, 0.3000)	—	—	10150	111
$CaLiLa\ (PO_4)_2:Dy^{3+}$	573	(0.2750, 0.3006)	—	—	—	112
$SrLu(PO_4)_3:Dy^{3+}$	575	(0.3740, 0.4070)	—	—	—	113
$K_3ZnB_5O_{10}:Dy^{3+}$	575	(0.2560, 0.2580)	—	—	—	114
$Y_2MoO_6:Dy^{3+}$	575	(0.3391, 0.3458)	91	—	5218	115
$Ca_2Al_2O_5:Dy^{3+}$	575	(0.3737, 0.3934)	57	69	4291	This work

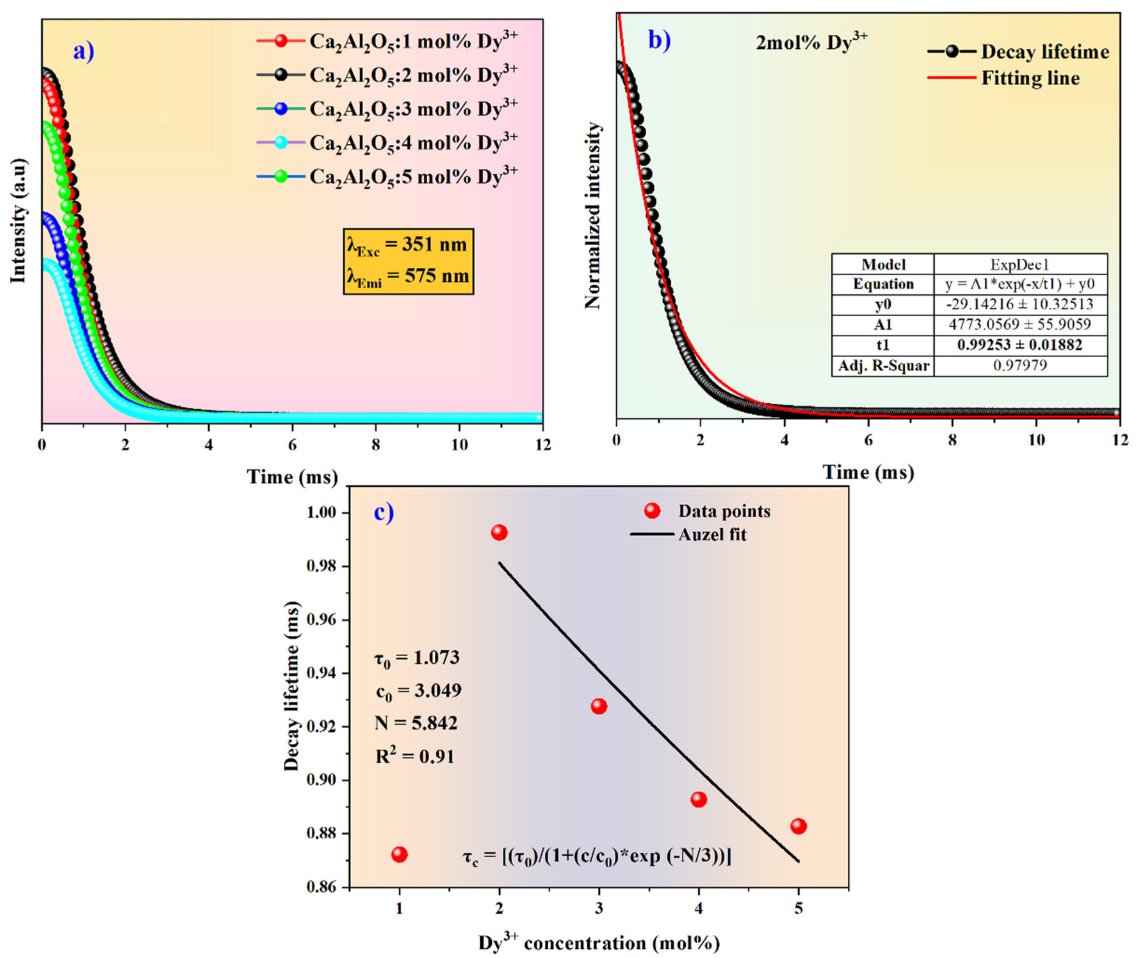

Fig. 10 (a) Fluorescence decay lifetime spectra for different concentration of Dy^{3+} in $Ca_2Al_2O_5$ phosphors. (b) Single exponential fit for the 2 mol% Dy^{3+}. (c) Auzel's fitting curve showing variation of fluorescence lifetime with Dy^{3+} concentrations.

Table 7 Decay time, non radiative relaxation rate and quantum efficiency of prepared $Ca_2Al_2O_5$:xDy^{3+} [x = 1, 2, 3, 4, and 5 mol%] phosphors

Dy^{3+} concentration (mol%)	τ_c (ms)	k_{nr} (s^{-1})	η (%)
1	0.87224	214.507	81.28
2	0.99253	75.55977	92.50
3	0.9276	146.0844	86.44
4	0.89284	188.0551	83.20
5	0.88279	200.8058	82.27

formation of defect states at higher temperatures, facilitating non-radiative relaxation routes. As a result, non-radiative recombination processes become more dominant than radiative ones, reducing emission intensity.[122] Fig. 11(b) illustrates the variation in normalized emission intensity at wavelengths of 483 nm, 575 nm, and 663 nm as a function of temperature. The normalized intensities exhibit a consistent decline, indicative of the quenching trend observed in the TDPL spectra, thereby confirming the temperature sensitivity of the luminescence process.

Notably, the emission peaks at 483 nm and 576 nm exhibit almost identical quenching behaviour, suggesting that thermal disturbances similarly affect these transitions and may originate from closely related energy levels within the Dy^{3+} ion.[123,124] Fig. 11(c) illustrates how the full width at half maximum (FWHM) of the same emission bands varies with temperature. As the temperature increases, the FWHM values for the 483 nm and 575 nm emissions increase, whereas the 663 nm emission experiences a narrowing of FWHM. The spectral broadening is correlated with the increased phonon interactions at higher temperatures. There are reported models explaining the spectral broadening and enhanced phonon interactions in rare earth-doped materials.[125] The dependence of FWHM on temperature is described using the following equation,

$$\Gamma = h\upsilon\sqrt{8\ln(2)S\coth\left(\frac{h\upsilon}{2kT}\right)} \quad (16)$$

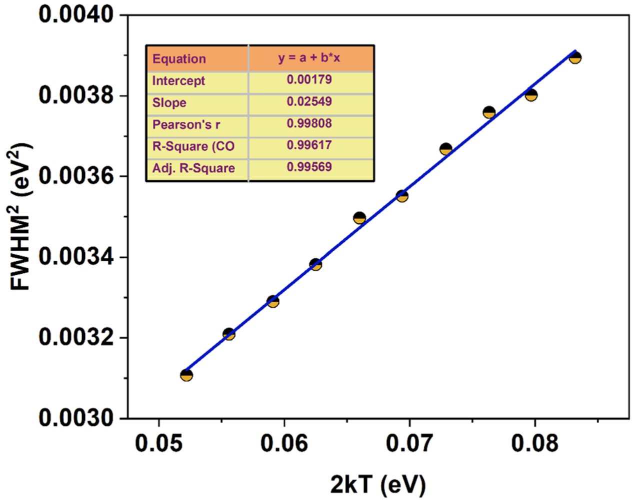

Fig. 12 The linear fit of $FWHM^2$ as a function of $2kT$ for 575 nm peak.

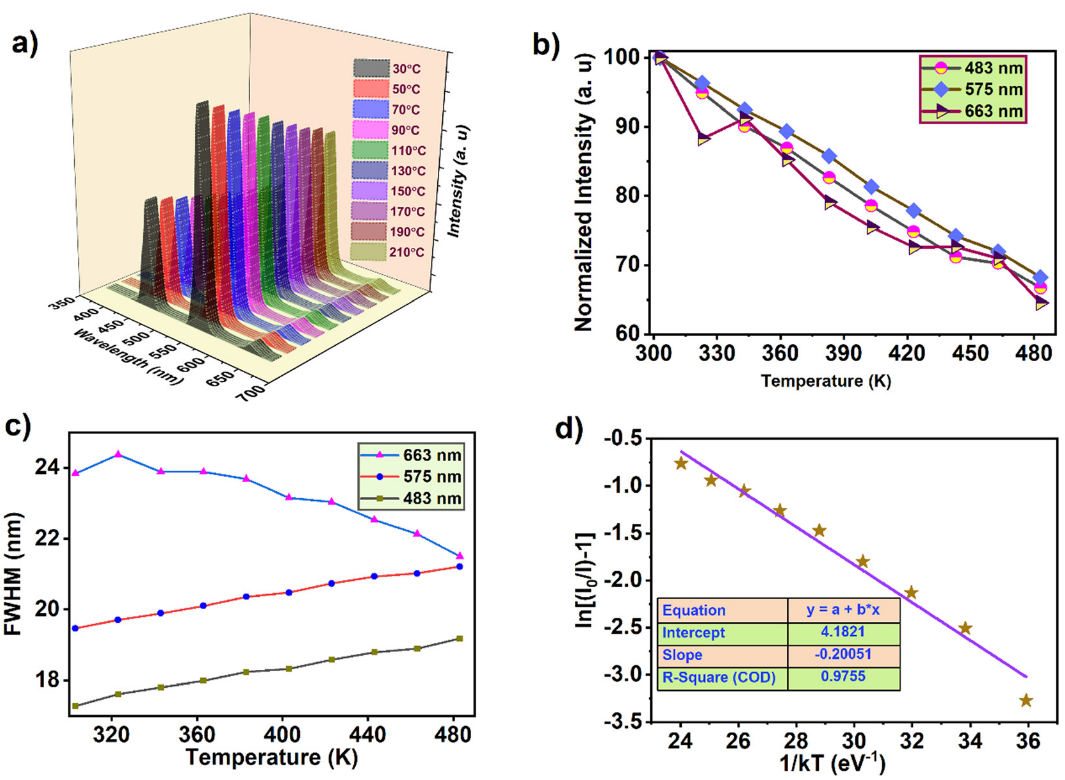

Fig. 11 (a) TDPL spectra of CAO–2 Dy sample, (b) normalized intensity variation, (c) FWHM variation for different emissions, and (d) activation energy graph of CAO–2 Dy phosphor.

Γ represents the full width at half maximum that varies with temperature, S is the Huang–Rhys parameter, k is the Boltzmann constant, $h\upsilon$ is the effective phonon energy, and T signifies the temperature. The extent of thermal quenching varies from one material to another. The thermal quenching is described as an effect of electron–phonon interaction. It depends on the phonon energy ($h\upsilon$) and S. If the phonon energy and S are larger, the stronger the electron–phonon interaction results in increased non-radiative relaxations. The thermal stability is associated with these values, and we simplify eqn (16) by expanding $\coth\left(\frac{h\upsilon}{2kT}\right)$ as $\frac{e^{\frac{h\upsilon}{2kT}}+e^{\frac{-h\upsilon}{2kT}}}{e^{\frac{h\upsilon}{2kT}}-e^{\frac{-h\upsilon}{2kT}}}$ and further simplified, and eqn (16) is squared,

$$\Gamma^2 = 5.57 \times S \times (h\upsilon)^2\left(1+\frac{2}{e^{\frac{h\upsilon}{kT}}-1}\right) \tag{17}$$

Approximating $\frac{h\upsilon}{kT} \approx 10^{-3}$ and $\left(e^{\frac{h\upsilon}{kT}}-1\right) \approx \frac{h\upsilon}{kT}$.

Eqn (17) is simplified into eqn (18),

$$\Gamma^2 = 5.57 \times S \times (h\upsilon)^2\left(1+\frac{1}{\frac{h\upsilon}{2kT}}\right) \tag{18}$$

Linearizing the above equation by taking $y = a + bx$, Γ^2 or FWHM^2 is taken along y-axis, kT along x-axis, $b = 5.57 \times S \times h\upsilon$, is the slope, and $a = 5.57 \times S \times (h\upsilon)^2$ is the intercept. Thus, the phonon energy and the S values are obtained by plotting the FWHM^2 *vs.* kT graph (Fig. 12). The phonon energy is 0.07022 eV, and S = 0.06517 for the 575 nm peak. On comparing the obtained values with the literature available, we can confirm that synthesized CAO–2 Dy samples show excellent thermal stability due to weaker electron–phonon interaction (lower value of S and $h\upsilon$).[126,127]

The activation energy must be calculated using the Arrhenius equation to explore the thermal quenching properties.[128]

$$I = \frac{I_0}{1+Ce^{\frac{-\Delta E}{kT}}} \tag{19}$$

The initial intensity is denoted as I_0 at the starting temperature, while I represent the intensity at temperature T. Here, C stands for a constant, ΔE signifies the activation energy, and k is the Boltzmann constant. On linearizing the equation,

$$\ln\left(\frac{I_0}{I}-1\right) = \frac{-\Delta E}{kT} + \ln C \tag{20}$$

The slope of $\ln\left(\frac{I_0}{I}-1\right)$ *versus* $\frac{1}{kT}$ graph (Fig. 11(d)) gives ΔE = 0.20051 eV.

Table 8 compares the reported systems with CAO–2 Dy phosphors regarding their thermal stability and activation energy. The data indicate that the CAO–2 Dy phosphor demonstrates superior thermal stability and activation energy, rendering it a promising candidate for optoelectronic applications.

Table 8 Comparison of optimized phosphor's thermal stability and activation energies with previously reported phosphors

Phosphor	Temperature range (K)	Thermal stability (%)	Activation energy (eV)	Ref.
$CaLiLa(PO_4)_2:Dy^{3+}$	303–553	65	0.250	112
$SrLu(PO_4)_3:Dy^{3+}$	298–473	68	0.214	113
$K_3ZnB_5O_{10}:Dy^{3+}$	303–483	82	0.520	114
$K_3Y(PO_4)_2:Dy^{3+}$	303–483	75	0.370	129
$LiCaBO_3:Dy^{3+}$	100–480	—	0.420	130
$Li_3Ba_2Gd_3(WO_4)_8:Dy^{3+}$	298–523	62	0.352	131
$Na_2Y_2TeB_2O_{10}:Dy^{3+}$	300–475	75	0.230	132
$NaGdTiO_4:Dy^{3+}$	298–633	—	0.200	133
$Y_2CaB_{10}O_{19}:Dy^{3+}$	303–663	84	—	134
$Ca_3LuAl_3B_4O_{15}:Dy^{3+}$	300–500	85	—	135
$Ca_2Al_2O_5:Dy^{3+}$	303–483	68	0.200	Present work

4. Conclusions

This work effectively synthesized $Ca_2Al_2O_5$ phosphors doped with Dy^{3+} through the conventional solid-state reaction technique. XRD analysis confirmed the formation of a pure phase, with no significant shifts in peak positions observed upon Dy^{3+} doping, indicating that the host lattice retained its structural integrity across all doping levels. SEM analysis of the surface morphology revealed agglomerated particle formations, characteristic of high-temperature solid-state synthesis processes. Optical characterization *via* DRS identified distinct Dy^{3+} absorption peaks and a reduction in the optical band gap upon introducing the dopant into the host matrix, underscoring the impact of Dy^{3+} incorporation. PL spectra exhibited the characteristic emission peaks of Dy^{3+} ions, corresponding to the $^4F_{9/2} \rightarrow {}^6H_{15/2}$ (blue) and $^4F_{9/2} \rightarrow {}^6H_{13/2}$ (yellow), and $^4F_{9/2} \rightarrow {}^6H_{11/2}$ (red) transitions. 2 mol% Dy^{3+} doping yielded the highest emission intensity, with chromaticity coordinates within the cool white light region, rendering it suitable for lighting applications. TDPL studies demonstrated significant thermal stability, with the phosphor maintaining substantial luminescence at elevated temperatures. The calculated activation energy was determined to be 0.200 eV, highlighting the lower probability for non-radiative losses. In conclusion, the exceptional optical properties, robust thermal stability, and emission in the visible white-light spectrum position make Dy^{3+}-doped $Ca_2Al_2O_5$ is identified as a promising phosphor candidate for applications in solid-state lighting and other optoelectronic devices.

Author contributions

Vidya Saraswathi. A: Conceptualization, Data curation, Formal analysis, Investigation, Methodology, Validation, Writing - original draft, Writing - review & editing; Tejas: Synthesis, Formal analysis, Writing, review; S. Masilla Moses Kennedy: Instrumentation, Formal analysis; A. Princy: Instrumentation, Formal analysis; M. I. Sayyed: Proofreading, Review & editing; Aljawhara. H. Almuqrin: Review & editing; Vikash Mishra: Formal analysis, Review & editing; Sudha. D. Kamath: Supervision, review and editing. All authors have read and agreed to the published version of the manuscript.

Conflicts of interest

There are no conflicts to declare.

Data availability

The data that support the findings of this study are available from the corresponding author upon reasonable request.

Acknowledgements

The authors express their gratitude to Princess Nourah bint Abdulrahman University Researchers Supporting Project number (PNURSP2025R2), Princess Nourah bint Abdulrahman University, Riyadh, Saudi Arabia.

References

1 S. Ye, F. Xiao, Y. X. Pan, Y. Y. Ma and Q. Y. Zhang, Phosphors in phosphor-converted white light-emitting diodes: recent advances in materials, techniques and properties, *Mater. Sci. Eng., R*, 2010, **71**, 1–34, DOI: 10.1016/j.mser.2010.07.001.

2 Y. Li, M. Gecevicius and J. Qiu, Long persistent phosphors – From fundamentals to applications, *Chem. Soc. Rev.*, 2016, **45**, 2090–2136, DOI: 10.1039/c5cs00582e.

3 Y. Pan, M. Wu and Q. Su, Comparative investigation on synthesis and photoluminescence of YAG:Ce phosphor, *Mater. Sci. Eng., B*, 2004, **106**, 251–256, DOI: 10.1016/j.mseb.2003.09.031.

4 A. C. Berends, M. A. Van De Haar and M. R. Krames, YAG:Ce^{3+} Phosphor: From Micron-Sized Workhorse for General Lighting to a Bright Future on the Nanoscale, *Chem. Rev.*, 2020, **120**, 13461–13479, DOI: 10.1021/acs.chemrev.0c00618.

5 Y. Hu, W. Zhuang, H. Ye, S. Zhang, Y. Fang and X. Huang, Preparation and luminescent properties of $(Ca_{1-x},Sr_x)S:Eu^{2+}$ red-emitting phosphor for white LED, *J. Lumin.*, 2005, **111**, 139–145, DOI: 10.1016/j.jlumin.2004.07.005.

6 R. Selomulya, S. Ski, K. Pita, C. H. Kam, Q. Y. Zhang and S. Buddhudu, Luminescence properties of $Zn_2SiO_4:Mn^{2+}$ thin-films by a sol–gel process, *Mater. Sci. Eng., B*, 2003, **100**, 136–141, DOI: 10.1016/S0921-5107(03)00084-9.

7 K. B. Kim, Y. Il Kim, H. G. Chun, T. Y. Cho, J. S. Jung and J. G. Kang, Structural and optical properties of $BaMgAl_{10}O_{17}:Eu^{2+}$ phosphor, *Chem. Mater.*, 2002, **14**, 5045–5052, DOI: 10.1021/cm020592f.

8 D. V. Sampaio, N. R. S. Souza, J. C. A. Santos, D. C. Silva, E. J. S. Fonseca, C. Kucera, B. Faugas, J. Ballato and R. S. Silva, Translucent and persistent luminescent $SrAl_2O_4:Eu^{2+},Dy^{3+}$ ceramics, *Ceram. Int.*, 2016, **42**, 4306–4312, DOI: 10.1016/j.ceramint.2015.11.108.

9 O. Arellano-Tánori, R. Meléndrez, M. Pedroza-Montero, B. Castañeda, V. Chernov, W. M. Yen and M. Barboza-Flores, Persistent luminescence dosimetric properties of UV-irradiated $SrAl_2O_4:Eu^{2+}$, Dy^{3+} phosphor, *J. Lumin.*, 2008, **128**, 173–184, DOI: 10.1016/j.jlumin.2007.07.006.

10 R. Aroz, V. Lennikov, R. Cases, M. L. Sanjuán, G. F. de la Fuente and E. Muñoz, Laser synthesis and luminescence properties of $SrAl_2O_4:Eu^{2+},Dy^{3+}$ phosphors, *J. Eur. Ceram. Soc.*, 2012, **32**, 4363–4369, DOI: 10.1016/j.jeurceramsoc.2012.06.013.

11 J. Tian and W. Zhuang, Thermal stability of nitride phosphors for light-emitting diodes, *Inorg. Chem. Front.*, 2021, **8**, 4933–4954, DOI: 10.1039/d1qi00993a.

12 Q. Wei, J. Ding and Y. Wang, A novel tunable extra-broad yellow-emitting nitride phosphor with zero-thermal-quenching property, *Chem. Eng. J.*, 2020, **386**, 124004, DOI: 10.1016/j.cej.2019.124004.

13 N. C. George, A. Birkel, J. Brgoch, B. C. Hong, A. A. Mikhailovsky, K. Page, A. Llobet and R. Seshadri, Average and local structural origins of the optical properties of the nitride phosphor $La_{3-x}Ce_xSi_6N_{11}$ ($0 < x = 3$), *Inorg. Chem.*, 2013, **52**, 13730–13741, DOI: 10.1021/ic402318k.

14 R. J. Xie, N. Hirosaki, M. Mitomo, K. Takahashi and K. Sakuma, Highly efficient white-light-emitting diodes fabricated with short-wavelength yellow oxynitride phosphors, *Appl. Phys. Lett.*, 2013, **52**, 13730–13741, DOI: 10.1063/1.2182067.

15 W. T. Chen, H. S. Sheu, R. S. Liu and J. P. Attfield, Cation-size-mismatch tuning of photoluminescence in oxynitride phosphors, *J. Am. Chem. Soc.*, 2012, **134**, 8022–8025, DOI: 10.1021/ja301593z.

16 J. Ding, Y. Wei, W. Liu, Y. Li, Q. Wu and J. Zhou, Highly efficient and thermally stable narrow-band cyan-emitting aluminum oxynitride phosphor for WLEDs and FEDs, *Chem. Eng. J.*, 2021, **403**, 126382, DOI: 10.1016/j.cej.2020.126382.

17 X. Xu, Q. Shao, L. Yao, Y. Dong and J. Jiang, Highly efficient and thermally stable Cr^{3+}-activated silicate phosphors for broadband near-infrared LED applications, *Chem. Eng. J.*, 2020, **383**, 123108, DOI: 10.1016/j.cej.2019.123108.

18 V. B. Bhatkar, S. K. Omanwar and S. V. Moharil, Combustion synthesis of silicate phosphors, *Opt. Mater.*, 2007, **29**, 1066–1070, DOI: 10.1016/j.optmat.2006.04.006.

19 M. Zhao, Q. Zhang and Z. Xia, Structural Engineering of Eu^{2+}-Doped Silicates Phosphors for LED Applications, *Acc. Mater. Res.*, 2020, **1**, 137–145, DOI: 10.1021/accountsmr.0c00014.

20 M. Kalidasan, K. Baskar and R. Dhanasekaren, Investigation of Er^{3+},Yb^{3+},Nd^{3+} doped yttrium calcium oxyborate for photon upconversion applications, *Solid State Sci.*, 2016, **57**, 9–15, DOI: 10.1016/j.solidstatesciences.2016.05.001.

21 L. C. Oliveira and O. Baffa, A new luminescent material based on CaB_6O_{10}:Pb to detect radiation, *J. Lumin.*, 2017, **181**, 171–178, DOI: 10.1016/j.jlumin.2016.09.009.

22 I.-E. Kwon, B.-Y. Yu, H. Bae, Y.-J. Hwang, T.-W. Kwon, C.-H. Kim, C.-H. Pyun and S.-J. Kim, Luminescence properties of borate phosphors in the UV/VUV region, *J. Lumin.*, 2000, **87–89**, 1039–1041.

23 V. Singh, V. Natarajan and J. J. Zhu, Studies on Eu doped Ba and Zn aluminate phosphors prepared by combustion synthesis, *Opt. Mater.*, 2007, **29**, 1447–1451, DOI: 10.1016/j.optmat.2006.07.003.

24 Z. Huang, B. Chen, B. Ren, D. Tu, Z. Wang, C. Wang, Y. Zheng, X. Li, D. Wang, Z. Ren, S. Qu, Z. Chen, C. Xu, Y. Fu and D. Peng, Smart Mechanoluminescent Phosphors: A Review of Strontium–Aluminate-Based Materials, Properties, and Their Advanced Application Technologies, *Adv. Sci.*, 2023, **10**, 2204925, DOI: **10.1002/advs.202204925**.

25 X. Chen, Z. Xia, M. Yi, X. Wu and H. Xin, Rare-earth free self-activated and rare-earth activated $Ca_2NaZn_2V_3O_{12}$ vanadate phosphors and their color-tunable luminescence properties, *J. Phys. Chem. Solids*, 2013, **74**, 1439–1443, DOI: **10.1016/j.jpcs.2013.05.002**.

26 D. Song, C. Guo and T. Li, Luminescence of the self-activated vanadate phosphors $Na_2LnMg_2V_3O_{12}$ (Ln = Y, Gd), *Ceram. Int.*, 2015, **41**, 6518–6524, DOI: **10.1016/j.ceramint.2015.01.094**.

27 P. Dang, D. Liu, Y. Wei, G. Li, H. Lian, M. Shang and J. Lin, Highly Efficient Cyan-Green Emission in Self-Activated $Rb_3RV_2O_8$ (R = Y, Lu) Vanadate Phosphors for Full-Spectrum White Light-Emitting Diodes (LEDs), *Inorg. Chem.*, 2020, **59**, 6026–6038, DOI: **10.1021/acs.inorgchem.0c00015**.

28 T. Leśniewski, Evolution of the full energy structure of Mn^{4+} in fluoride phosphors under high pressure conditions, *Phys. Chem. Chem. Phys.*, 2023, **25**, 14449–14462, DOI: **10.1039/d3cp01045g**.

29 Y. H. Kim, J. Ha and W. Bin Im, Towards green synthesis of Mn^{4+}-doped fluoride phosphors: a review, *J. Mater. Res. Technol.*, 2021, **11**, 181–195, DOI: **10.1016/j.jmrt.2021.01.011**.

30 M. Ye, C. Yang, A. Wang, G. Chen, D. Yuan and W. Zhou, Advancing Red-Emitting Fluoride Phosphors for Highly Stable White Light-Emitting Diodes: Crystal Reconstruction and Covalence Enhancement Strategy, *Inorg. Chem.*, 2023, **62**, 12130–12137, DOI: **10.1021/acs.inorgchem.3c01709**.

31 C.-T. Yeh, Y.-I. Chou, K.-S. Yang, S.-K. Wu and C.-C. Wang, Luminescence material characterizations on laser-phosphor lighting techniques, *Opt. Express*, 2019, **27**, 7226, DOI: **10.1364/oe.27.007226**.

32 C. Cozzan, G. Lheureux, N. O'Dea, E. E. Levin, J. Graser, T. D. Sparks, S. Nakamura, S. P. Denbaars, C. Weisbuch and R. Seshadri, Stable, Heat-Conducting Phosphor Composites for High-Power Laser Lighting, *ACS Appl. Mater. Interfaces*, 2018, **10**, 5673–5681, DOI: **10.1021/acsami.8b00074**.

33 J. Y. Cho, K. Y. Ko and Y. R. Do, Optical properties of sol–gel derived Y_2O_3:Eu^{3+} thin-film phosphors for display applications, *Thin Solid Films*, 2007, **515**, 3373–3379, DOI: **10.1016/j.tsf.2006.09.029**.

34 R. P. Rao, Tb[sup3+] Activated Green Phosphors for Plasma Display Panel Applications, *J. Electrochem. Soc.*, 2003, **150**, H165, DOI: **10.1149/1.1583718**.

35 S. Tripathi, R. Tiwari, A. K. Shrivastava, V. K. Singh, N. Dubey and V. Dubey, A review reports on rare earth activated $AZrO_3$ (A = Ba, Ca, Sr) phosphors for display and sensing applications, *Optik*, 2018, **157**, 365–381, DOI: **10.1016/j.ijleo.2017.11.017**.

36 W. Wang, S. Yan, Y. Liang, D. Chen, F. Wang, J. Liu, Y. Zhang, K. Sun and D. Tang, A red-light-chargeable near infrared $MgGeO_3$:Mn^{2+},Yb^{3+} persistent phosphor for bioimaging and optical information storage applications, *Inorg. Chem. Front.*, 2021, **8**, 5149–5157, DOI: **10.1039/d1qi01158h**.

37 Y. Wei and J. Wang, X-ray/γ-ray/Ultrasound-Activated Persistent Luminescence Phosphors for Deep Tissue Bioimaging and Therapy, *ACS Appl. Mater. Interfaces*, 2024, **16**, 56519–56544, DOI: **10.1021/acsami.4c11585**.

38 H. Suo, C. Guo and T. Li, Broad-Scope Thermometry Based on Dual-Color Modulation up-Conversion Phosphor $Ba_5Gd_8Zn_4O_{21}$:Er^{3+}/Yb^{3+}, *J. Phys. Chem. C*, 2016, **120**, 2914–2924, DOI: **10.1021/acs.jpcc.5b11786**.

39 N. Tyagi, A. A. Reddy and R. Nagarajan, $KLaF_4$:Er an efficient upconversion phosphor, *Opt. Mater.*, 2010, **33**, 42–47, DOI: **10.1016/j.optmat.2010.07.014**.

40 F. Huang, Y. Gao, J. Zhou, J. Xu and Y. Wang, Yb^{3+}/Er^{3+} co-doped $CaMoO_4$: a promising green upconversion phosphor for optical temperature sensing, *J. Alloys Compd.*, 2015, **639**, 325–329, DOI: **10.1016/j.jallcom.2015.02.228**.

41 J. M. Kalita and M. L. Chithambo, Phosphorescence of beta irradiated $Sr_4Al_{14}O_{25}$:Eu^{2+},Dy^{3+} – A persistent luminescence phosphor, *J. Lumin.*, 2024, **272**, 120664, DOI: **10.1016/j.jlumin.2024.120664**.

42 N. Zhang, Y. T. Tsai, M. H. Fang, C. G. Ma, A. Lazarowska, S. Mahlik, M. Grinberg, C. Y. Chiang, W. Zhou, J. G. Lin, J. F. Lee, J. Zheng, C. Guo and R. S. Liu, Aluminate Red Phosphor in Light-Emitting Diodes: Theoretical Calculations, Charge Varieties, and High-Pressure Luminescence Analysis, *ACS Appl. Mater. Interfaces*, 2017, **9**, 23995–24004, DOI: **10.1021/acsami.7b06840**.

43 P. J. Dereń, D. Sztolberg, B. Brzostowski and B. Bondzior, Spectroscopic properties and Judd–Ofelt analysis of $LaAlO_3$ monocrystal doped with Tm^{3+} ions, *J. Lumin.*, 2016, **178**, 400–406, DOI: **10.1016/j.jlumin.2016.05.049**.

44 Z. Fu and B. Liu, Solution combustion synthesis, photoluminescence and X-ray luminescence of Eu^{3+}-doped $LaAlO_3$ nanophosphors, *Ceram. Int.*, 2016, **42**, 2357–2363, DOI: **10.1016/j.ceramint.2015.10.032**.

45 M. Ayvacikli, A. Ege and N. Can, Radioluminescence of $SrAl_2O_4$:Ln^{3+} (Ln = Eu, Sm, Dy) phosphor ceramic, *Opt. Mater.*, 2011, **34**, 138–142, DOI: **10.1016/j.optmat.2011.07.023**.

46 M. Ayvacikli, A. Ege, S. Yerci and N. Can, Synthesis and optical properties of Er^3 and Eu^3 doped $SrAl_2O_4$ phosphor ceramic, *J. Lumin.*, 2011, **131**, 2432–2439, DOI: **10.1016/j.jlumin.2011.05.051**.

47 T. Qi, H. Xia, Z. Zhang, S. Kong, W. Peng, Q. Zhao and Z. Huang, Improved water resistance of $SrAl_2O_4$:Eu^{2+},Dy^{3+} phosphor directly achieved in a water-containing medium, *Solid State Sci.*, 2017, **65**, 88–94, DOI: **10.1016/j.solidstatesciences.2017.01.006**.

48 R. Aroz, V. Lennikov, R. Cases, M. L. Sanjuán, G. F. de la Fuente and E. Muñoz, Laser synthesis and luminescence properties of $SrAl_2O_4$:Eu^{2+},Dy^{3+} phosphors, *J. Eur. Ceram. Soc.*, 2012, **32**, 4363–4369, DOI: **10.1016/j.jeurceramsoc.2012.06.013**.

49 T. Cui, P. Ma, Y. Sheng, K. Zheng, X. Zhou, C. Xu, H. Zou and Y. Song, Preparation of $CaAl_2O_4$:Eu^{2+},Nd^{3+} and

$SrAl_2O_4:Eu^{2+},Dy^{3+}$ long afterglow luminescent materials using oil shale ash, *Opt. Mater.*, 2017, **67**, 84–90, DOI: 10.1016/j.optmat.2017.03.052.

50 M. Freeda and T. D. Subash, Preparation and Characterization of Praseodymium doped Calcium Aluminate nanophosphor ($CaAl_2O_4$:Pr) by sol–gel method, *Mater. Today: Proc.*, 2017, **4**, 4266–4273, DOI: 10.1016/j.matpr.2017.02.130.

51 B. S. Shashikala, H. B. Premkumar, G. P. Darshan, H. Nagabhushana, S. C. Sharma, S. C. Prashantha and H. P. Nagaswarupa, Synthesis and Photoluminescence Studies of an Orange Red Color Emitting novel $CaAl_2O_4:Sm^{3+}$ nanophosphor for LED Applications, *Mater. Today: Proc.*, 2017, **4**, 11820–11826, DOI: 10.1016/j.matpr.2017.09.100.

52 M. N. Singh, L. R. Singh and A. G. Barua, Effects of doping concentration on thermoluminescence parameters of $CaAl_2O_4:Re^{3+}$ (Re^{3+} = Dy^{3+}, Sm^{3+}, Tm^{3+}) prepared by combustion method, *Radiat. Phys. Chem.*, 2021, **188**, 109631, DOI: 10.1016/j.radphyschem.2021.109631.

53 D. Jia, X.-J. Wang and W. M. Yen, Electron traps in Tb^{3+}-doped $CaAl_2O_4$, *Chem. Phys. Lett.*, 2002, **363**, 241–244, DOI: 10.1016/S0009-2614(02)01170-3.

54 V. Singh, R. P. S. Chakradhar, J. L. Rao and H. Y. Kwak, Enhanced blue emission and EPR study of $LaMgAl_{11}O_{19}$:Eu phosphors, *J. Lumin.*, 2011, **131**, 247–252, DOI: 10.1016/j.jlumin.2010.10.006.

55 Ü. H. Kaynar, S. C. Kaynar, M. Ayvacikli, Y. Karabulut, G. O. Souadi and N. Can, Influence of laser excitation power on temperature-dependent luminescence behaviour of Ce- and Tb-incorporated $BaMgAl_{10}O_{17}$ phosphors, *Radiat. Phys. Chem.*, 2020, **168**, 108617, DOI: 10.1016/j.radphyschem.2019.108617.

56 K. B. Kim, K. W. Koo, T. Y. Cho and H. G. Chun, Effect of heat treatment on photoluminescence behavior of $BaMgAl_{10}O_{17}$:Eu phosphors, *Mater. Chem. Phys.*, 2003, **80**, 682–689, DOI: 10.1016/S0254-0584(03)00110-X.

57 N. Pradal, A. Potdevin, G. Chadeyron, P. Bonville, B. Caillier and R. Mahiou, Spectroscopic study and enhanced thermostability of combustion-derived $BaMgAl_{10}O_{17}:Eu^{2+}$ blue phosphors for solid-state lighting, *Opt. Mater.*, 2017, **64**, 334–344, DOI: 10.1016/j.optmat.2016.12.031.

58 C. Shen, Y. Yang, S. Jin and J. Ming, Luminous characteristics and thermal stability of $BaMgAl_{10}O_{17}:Eu^{2+}$ phosphor for white light-emitting diodes, *Phys. B*, 2010, **405**, 1045–1049, DOI: 10.1016/j.physb.2009.10.055.

59 L. You, R. Tian, T. Zhou and R. J. Xie, Broadband near-infrared phosphor $BaMgAl_{10}O_{17}:Cr^{3+}$ realized by crystallographic site engineering, *Chem. Eng. J.*, 2021, **417**, 129224, DOI: 10.1016/j.cej.2021.129224.

60 M. Kumar, P. Rajput, P. K. Singh, A. C. Yadav, S. L. Pradhan, V. Baranwal, U. B. Singh, S. N. Jha and F. Singh, Luminescence properties of $BaMgAl_{10}O_{17}:Mn^{2+}$ nanophosphors, *J. Alloys Compd.*, 2019, **799**, 556–562, DOI: 10.1016/j.jallcom.2019.05.332.

61 L. Wu, X. Tian, X. Wei, Y. Chen and M. Yin, Photoluminescence studies of Eu^{2+}–Yb^{3+} co-doped $BaMgAl_{10}O_{17}$ phosphor synthesized by the combustion method, *J. Rare Earths*, 2012, **30**, 1213–1216, DOI: 10.1016/S1002-0721(12)60208-7.

62 A. Vidya Saraswathi, T. Chennappa, K. Naregundi, A. Princy, S. M. M. Kennedy, A. S. Altowyan, M. I. Sayyed and S. D. Kamath, Unveiling highly sensitive Dy^{3+} doped $BaMgAl_{10}O_{17}$ phosphor's thermoluminescence trap features and temperature dependent luminescence for solid state lighting applications, *Phys. Scr.*, 2024, **99**, 085909, DOI: 10.1088/1402-4896/ad5876.

63 T. Wanjun, C. Donghua and W. Ming, Luminescence studies on $SrMgAl_{10}O_{17}$:Eu,Dy phosphor crystals, *Opt. Laser Technol.*, 2009, **41**, 81–84, DOI: 10.1016/j.optlastec.2008.03.009.

64 G. Ju, Y. Hu, L. Chen and X. Wang, Photoluminescence properties of color-tunable $SrMgAl_{10}O_{17}:Eu^{2+},Mn^{2+}$ phosphors for UV LEDs, *J. Lumin.*, 2012, **132**, 1792–1797, DOI: 10.1016/j.jlumin.2012.02.036.

65 A. Nande, A. N. Yerpude and S. J. Dhoble, Estimation of Judd–Ofelt Parameters for Eu^{3+}-Doped $Ca_3B_2O_6$, $Ca_2Al_2O_5$, and $Sr_3SiO_4Cl_6$ Host Materials, *J. Electron. Mater.*, 2025, **54**, 1327–1334, DOI: 10.1007/s11664-024-11631-7.

66 A. N. Yerpude, V. R. Panse, S. J. Dhoble, N. S. Kokode and M. Srinivas, Photoluminescence properties of $Ca_2Al_2O_5:RE^{3+}$ (RE = Eu, Dy and Tb) phosphors for solid state lighting, *Luminescence*, 2017, **32**, 1361–1364, DOI: 10.1002/bio.3340.

67 A. Verma and A. Verma, Synthesis, characterization, mechanoluminescence, thermoluminescence, and antibacterial properties of $SrMgAl_{10}O_{17}$:Eu phosphor, *J. Alloys Compd.*, 2019, **802**, 394–408, DOI: 10.1016/j.jallcom.2019.06.209.

68 L. A. Xue, Y. Chent and R. J. Brook, The Influence of Ionic Radii on the Incorporation of Trivalent Dopants into $BaTiO_3$, *Mater. Sci. Eng. B.*, 1988, **1**(2), 193–201, DOI: 10.1016/0921-5107(88)90019-0.

69 R. D. Shannon, Revised Effective Ionic Radii and Systematic Studies of Interatomie Distances in Halides and Chaleogenides, *Acta Crystallogr., Sect. A*, 1976, **32**, 751–767, DOI: 10.1107/S0567739476001551.

70 M. Schmidt, T. Stumpf, M. M. Fernandes, C. Walther and T. Fanghänel, Charge compensation in solid solutions, *Angew. Chem., Int. Ed.*, 2008, **47**, 5846–5850, DOI: 10.1002/anie.200705827.

71 P. Kumar, D. Singh, S. Kadyan, H. Kumar and R. Kumar, Comprehensive investigation of $Y_2Si_2O_7:Eu^{3+}$ nanophosphors for w-LEDs: structural, Judd–Ofelt calculation and photoluminescent characteristic with high color purity and thermal stability, *Ceram. Int.*, 2024, **50**, 34596–34608, DOI: 10.1016/j.ceramint.2024.06.267.

72 L. Alexander and H. P. Klug, Determination of crystallite size with the X-ray spectrometer, *J. Appl. Phys.*, 1950, **21**, 137–142, DOI: 10.1063/1.1699612.

73 A. Weibel, R. Bouchet, F. Boulc'h and P. Knauth, The big problem of small particles: a comparison of methods for determination of particle size in nanocrystalline anatase powders, *Chem. Mater.*, 2005, **17**, 2378–2385, DOI: 10.1021/cm0403762.

74 H. H. Tian and M. Atzmon, Comparison of X-ray analysis methods used to determine the grain size and strain in

nanocrystalline materials, *Philos. Mag. A*, 1999, **79**, 1769–1786, DOI: 10.1080/01418619908210391.

75 H. Kaur, M. Jayasimhadri, M. K. Sahu, P. K. Rao and N. S. Reddy, Synthesis of orange emitting Sm^{3+} doped sodium calcium silicate phosphor by sol–gel method for photonic device applications, *Ceram. Int.*, 2020, **46**, 26434–26439, DOI: 10.1016/j.ceramint.2020.04.224.

76 B. C. Jamalaiah and Y. Ramesh Babu, Near UV excited $SrAl_2O_4:Dy^{3+}$ phosphors for white LED applications, *Mater. Chem. Phys.*, 2018, **211**, 181–191, DOI: 10.1016/j.matchemphys.2018.02.025.

77 D. N. Game, N. B. Ingale and S. K. Omanwar, Synthesis and photoluminescence properties of $NaCaPO_4:Eu^{2+}$ phosphor for solid state lighting, *Optik*, 2016, **127**, 6204–6209, DOI: 10.1016/j.ijleo.2016.04.062.

78 H. S. Huang and Z. H. Liu, Enhanced photoluminescence property of $CaB_2O_4:Eu^{3+}$ phosphor prepared by calcining the $Ca_4B_{10}O_{19}{\cdot}7H_2O:Eu^{3+}$ precursor, *Mater. Res. Bull.*, 2014, **49**, 88–93, DOI: 10.1016/j.materresbull.2013.08.010.

79 S. P. Tandon and P. C. Mehta, Study of some Pr(III) complexes: interelectronic repulsion, spin–orbit interaction, and bonding, *J. Chem. Phys.*, 1970, **52**, 5424–5434, DOI: 10.1063/1.1672792.

80 W. T. Carnall, P. R. Fields and K. Rajnak, Electronic energy levels of the trivalent lanthanide aquo ions. IV. Eu^{8+}, *J. Chem. Phys.*, 1968, **49**, 4424–4442, DOI: 10.1063/1.1669893.

81 K. J. Albert, E. A. Rathnakumari and S. M. M. Kennedy, Synthesis, photoluminescent properties, and an insight into the Judd–Ofelt analysis of the $NaPbBi_{(2-x)}(PO_4)_3:xEu^{3+}$ orthophosphate phosphors for light applications, *J. Alloys Compd.*, 2023, **934**, 168047, DOI: 10.1016/j.jallcom.2022.168047.

82 R. Kiran, A. Princy, S. Masilla Moses Kennedy, V. Mishra, M. I. Sayyed, M. Rashad and S. D. Kamath, Evaluation of luminescent and thermal properties of Dy^{3+} doped tungstate phosphors for optoelectronic and thermometry applications, *Phys. B*, 2025, **697**, 416712, DOI: 10.1016/j.physb.2024.416712.

83 K. Linganna and C. K. Jayasankar, Optical properties of Eu^{3+} ions in phosphate glasses, *Spectrochim. Acta, Part A*, 2012, **97**, 788–797, DOI: 10.1016/j.saa.2012.07.031.

84 J. Torrent and V. Barrón, *Diffuse Reflectance Spectroscopy*, 2008.

85 P. Makuła, M. Pacia and W. Macyk, How To Correctly Determine the Band Gap Energy of Modified Semiconductor Photocatalysts Based on UV-Vis Spectra, *J. Phys. Chem. Lett.*, 2018, **9**, 6814–6817, DOI: 10.1021/acs.jpclett.8b02892.

86 H. F. Devi, K. T. Devi and T. D. Singh, Synthesis, Characterization, Optical and Electrical Properties of Citrate Mediated Terbium Doped ZnO Nanoparticles for Multifunctional Applications, *Integr. Ferroelectr.*, 2020, **204**, 81–89, DOI: 10.1080/10584587.2019.1674976.

87 N. Aggarwal, A. Vasishth, K. Kaur and N. K. Verma, Investigation of optical, electrical and magnetic properties of Tb-doped ZnO nanorods, *J. Mater. Sci.: Mater. Electron.*, 2019, **30**, 4807–4812, DOI: 10.1007/s10854-019-00774-7.

88 G. H. Mhlongo, O. M. Ntwaeaborwa, H. C. Swart, R. E. Kroon, P. Solarz, W. Ryba-Romanowski and K. T. Hillie, Luminescence dependence of Pr^{3+} activated SiO_2 nanophosphor on Pr^{3+} concentration, temperature, and ZnO incorporation, *J. Phys. Chem. C*, 2011, **115**, 17625–17632, DOI: 10.1021/jp201142d.

89 S. Saha, H. J. Kim, A. Khan, J. Cho, S. Kang and A. V. Ntarisa, Synthesis and luminescence studies of Dy^{3+} doped $Li_3Sc(BO_3)_2$ polycrystalline powder for warm white light, *Ceram. Int.*, 2022, **48**, 10667–10676, DOI: 10.1016/j.ceramint.2021.12.281.

90 T. Krishnapriya, A. Jose, T. Anna Jose, C. Joseph, N. V. Unnikrishnan and P. R. Biju, Luminescent kinetics of Dy^{3+} doped $CaZn_2(PO_4)_2$ phosphors for white light emitting applications, *Adv. Powder Technol.*, 2021, **32**, 1023–1032, DOI: 10.1016/j.apt.2021.02.003.

91 Y. Zhang, W. Gong, J. Yu, H. Pang, Q. Song and G. Ning, A new single-phase white-light-emitting $CaWO_4:Dy^{3+}$ phosphor: synthesis, luminescence and energy transfer, *RSC Adv.*, 2015, **5**, 62527–62533, DOI: 10.1039/c5ra12502b.

92 S. Saha, H. J. Kim, A. Khan, J. Cho, S. Kang and A. V. Ntarisa, Synthesis and luminescence studies of Dy^{3+} doped $Li_3Sc(BO_3)_2$ polycrystalline powder for warm white light, *Ceram. Int.*, 2022, **48**, 10667–10676, DOI: 10.1016/j.ceramint.2021.12.281.

93 W. Tang, Q. Guo, K. Su, H. Liu, Y. Zhang, L. Mei and L. Liao, Structure and Photoluminescence Properties of Dy^{3+} Doped Phosphor with Whitlockite Structure, *Materials*, 2022, **15**, 2177, DOI: 10.3390/ma15062177.

94 A. K. Bedyal, A. K. Kunti, V. Kumar and H. C. Swart, Effects of cationic substitution on the luminescence behavior of Dy^{3+} doped orthophosphate phosphor, *J. Alloys Compd.*, 2019, **806**, 1127–1137, DOI: 10.1016/j.jallcom.2019.07.305.

95 D. L. Dexter and J. H. Schulman, Theory of concentration quenching in inorganic phosphors, *J. Chem. Phys.*, 1954, **22**, 1063–1070, DOI: 10.1063/1.1740265.

96 J. Guo, S. Li, J. Kong, Y. Li, L. Zhou, L. Lou, Q. Lv, R. Tang, L. Zheng, B. Deng and R. Yu, Synthesis and characterization of a new double perovskite phosphor: $NaCaTiTaO_6:Dy^{3+}$ with high thermal stability for w-LEDs application, *Opt. Laser Technol.*, 2022, **155**, 108347, DOI: 10.1016/j.optlastec.2022.108347.

97 Y. Hua, H. Li, Z. Wu, L. Li and J. S. Yu, Double-perovskite structure-driven thermal-stabilized Dy^{3+}-activated yellow-emitting phosphors, *J. Alloys Compd.*, 2023, **968**, 171701, DOI: 10.1016/j.jallcom.2023.171701.

98 L. Yan, G. Zhu, S. Ma, S. Li, Z. Li, X. Luo and B. Dong, Emerging Fe^{3+} Doped Broad NIR-Emitting Phosphor $Ca_{2.5}Hf_{2.5}(Ga,Al)_3O_{12}:Fe^{3+}$ for LWUV Pumped NIR LED, *Laser Photonics Rev.*, 2024, **18**, 2301200, DOI: 10.1002/lpor.202301200.

99 S. Li, Q. Zhu, J. Xiahou and J. G. Li, Doping Pb^{2+} in $LaAlO_3$ to generate dual emission centers and an optical storage container for visible and near infrared persistent luminescence, *Dalton Trans.*, 2022, **51**, 1112–1122, DOI: 10.1039/d1dt03421a.

100 A. Santana-Alonso, A. C. Yanes, J. Méndez-Ramos, J. Del-Castillo and V. D. Rodríguez, Down-shifting by energy

transfer in Dy^{3+}–Tb^{3+} co-doped YF3-based sol–gel nano-glass-ceramics for photovoltaic applications, *Opt. Mater.*, 2011, **33**, 587–591, DOI: 10.1016/j.optmat.2010.10.040.

101 P. Haritha, I. R. Martín, K. Linganna, V. Monteseguro, P. Babu, S. F. León-Luis, C. K. Jayasankar, U. R. Rodríguez-Mendoza, V. Lavín and V. Venkatramu, Optimizing white light luminescence in Dy^{3+}-doped $Lu_3Ga_5O_{12}$ nano-garnets, *J. Appl. Phys.*, 2014, **116**, 174308, DOI: 10.1063/1.4900989.

102 Y. Hua, H. Li, Z. Wu, L. Li and J. S. Yu, Double-perovskite structure-driven thermal-stabilized Dy^{3+}-activated yellow-emitting phosphors, *J. Alloys Compd.*, 2023, **968**, 171701, DOI: 10.1016/j.jallcom.2023.171701.

103 S. Dutta, S. Som and S. K. Sharma, Luminescence and photometric characterization of K^+ compensated $CaMoO_4$:Dy^{3+} nanophosphors, *J. Chem. Soc., Dalton Trans.*, 2013, **42**, 9654–9661, DOI: 10.1039/c3dt50780g.

104 H. Guo, X. Huang and Y. Zeng, Synthesis and photoluminescence properties of novel highly thermal-stable red-emitting $Na_3Sc_2(PO_4)_3$:Eu^{3+} phosphors for UV-excited white-light-emitting diodes, *J. Alloys Compd.*, 2018, **741**, 300–306, DOI: 10.1016/j.jallcom.2017.12.316.

105 M. Shaw and M. Fairchild, Evaluating the 1931 CIE color-matching functions, *Color Res. Appl.*, 2002, **27**, 316–329, DOI: 10.1002/col.10077.

106 R. Song, Y. Zheng, H. Li, Y. Mao, K. Xiong and J. Zhu, Charge compensation and solid-state lighting application for dysprosium-activated $Ba_2TeP_2O_9$ phosphor, *J. Alloys Compd.*, 2022, **912**, 165188, DOI: 10.1016/j.jallcom.2022.165188.

107 T. Krishnapriya, A. Jose, T. Anna Jose, C. Joseph, N. V. Unnikrishnan and P. R. Biju, Luminescent kinetics of Dy^{3+} doped $CaZn_2(PO_4)_2$ phosphors for white light emitting applications, *Adv. Powder Technol.*, 2021, **32**, 1023–1032, DOI: 10.1016/j.apt.2021.02.003.

108 M. Behera, R. Panda, R. Arun Kumar, N. K. Mishra, K. Kumar and T. Del Monte, Microwave-assisted combustion synthesis and characterization studies of novel dysprosium doped yttrium calcium borate (Dy^{3+}:$Y_2CaB_{10}O_{19}$) phosphor materials for efficient white light applications, *Ceram. Int.*, 2024, **50**, 18146–18156, DOI: 10.1016/j.ceramint.2024.02.298.

109 S. Som, S. K. Sharma and S. P. Lochab, Ion induced modification of bandgap and CIE parameters in Y_2O_3:Dy^{3+} phosphor, *Ceram. Int.*, 2013, **39**, 7693–7701, DOI: 10.1016/j.ceramint.2013.03.022.

110 P. Kumar, D. Singh, I. Gupta and H. Kumar, Influence of Dy^{3+} ion concentration on structural, photoluminescence and energy transfer mechanism of promising $GdSr_2AlO_5$ nanophosphors for white light applications, *Ceram. Int.*, 2023, **49**, 29010–29024, DOI: 10.1016/j.ceramint.2023.06.173.

111 Y. Li, J. Chen and C. Chen, Tunable correlated color temperature of $NaSrPO_4$ phosphors via Dy^{3+} and Eu^{3+} co-doping for warm white light-emitting diodes, *Optik*, 2018, **174**, 1–6, DOI: 10.1016/j.ijleo.2018.08.055.

112 W. Tang, Q. Guo, K. Su, H. Liu, Y. Zhang, L. Mei and L. Liao, Structure and Photoluminescence Properties of Dy^{3+} Doped Phosphor with Whitlockite Structure, *Materials*, 2022, **15**, 2177, DOI: 10.3390/ma15062177.

113 T. Wang, Y. Hu, L. Chen, X. Wang and M. He, An intense single-component warm-white-light $Sr_3Lu(PO_4)_3$:Dy^{3+} phosphor for white UV-LEDs, *J. Mater. Sci.: Mater. Electron.*, 2016, **27**, 13235–13241, DOI: 10.1007/s10854-016-5470-9.

114 G. R. Dillip, G. B. Kumar, V. R. Bandi, M. Hareesh, B. Deva Prasad Raju, S. W. Joo, L. K. Bharat and J. S. Yu, Versatile host-sensitized white light emission in a single-component $K_3ZnB_5O_{10}$:Dy^{3+} phosphor for ultraviolet converted light-emitting diodes, *J. Alloys Compd.*, 2017, **699**, 1108–1117, DOI: 10.1016/j.jallcom.2017.01.008.

115 K. R. Bhagya, R. B. Basavaraj, K. R. Jyothi, H. Nagabhushana, M. V. Murugendrappa, A. P. G. Prakash, N. M. Nagabhushana and V. N. Hegde, Dy^{3+} doped Y_2MoO_6 nanopowders for white light emission: spectroscopic and transport properties for optoelectronic and energy harvesting applications, *Colloids Interface Sci. Commun.*, 2021, **43**, 100447, DOI: 10.1016/j.colcom.2021.100447.

116 P. Rohilla and A. S. Rao, Linear and non-linear photoluminescence studies of Ho^{3+}/Yb^{3+} co-doped titanate phosphors for photonic applications, *J. Alloys Compd.*, 2022, **928**, 167156, DOI: 10.1016/j.jallcom.2022.167156.

117 P. Rohilla, A. Prasad and A. Srinivasa Rao, Structural and luminescence studies on thermally stable Bi^{3+}-activated Ba_3MoTiO_8 phosphors for near UV-pumped w-LED applications, *Int. J. Appl. Ceram. Technol.*, 2024, **21**, 1208–1219, DOI: 10.1111/ijac.14580.

118 S. Kaur, H. Kaur and A. S. Rao, UV and blue excited tunable emission of thermally stable Bi^{3+} sensitized Eu^{3+} doped calcium aluminozincate phosphor for photonic applications, *Spectrochim. Acta, Part A*, 2024, **305**, 123524, DOI: 10.1016/j.saa.2023.123524.

119 I. Gupta, D. Singh, S. Singh, P. Kumar, S. Bhagwan and V. Kumar, Study of structural and spectroscopic characteristics of novel color tunable yellowish-white Dy^{3+} doped $Gd_4Al_2O_9$ nanophosphors for NUV-based WLEDs, *J. Mol. Struct.*, 2023, **1272**, 134199, DOI: 10.1016/j.molstruc.2022.134199.

120 S. Kaushik, S. Devi, M. Kumar, H. Dalal, A. Srivastava and M. Srivastava, Opto-electronic, crystallographic, and Judd–Ofelt analysis of novel gadolinium-based europium doped $BaSrGd_4O_8$ nanophosphor for advanced pc-WLEDs, *Mater. Res. Bull.*, 2022, **126**, 111966, DOI: 10.1016/j.materresbull.2022.111966.

121 R. A. Talewar, S. Mahamuda, K. Swapna, M. Venkateswarlu and A. S. Rao, Spectroscopic studies of Sm^{3+} ions doped alkaline-earth chloro borate glasses for visible photonic applications, *Mater. Res. Bull.*, 2018, **105**, 45–54, DOI: 10.1016/j.materresbull.2018.04.033.

122 L. Yan, B. Li, Y. Song, Z. Lv, X. Zheng, Q. Wu and Y. Yang, Optical temperature sensing using the multiphonon-assisted anti-Stokes-to-Stokes fluorescence intensity ratio, *Opt. Lett.*, 2017, **42**, 3793, DOI: 10.1364/ol.42.003793.

123 X. Yuan, X. Hou, J. Li, C. Qu, W. Zhang, J. Zhao and H. Li, Thermal degradation of luminescence in inorganic perovskite $CsPbBr_3$ nanocrystals, *Phys. Chem. Chem. Phys.*, 2017, **19**, 8934–8940, DOI: 10.1039/c6cp08824d.

124 C. Wei, D. Xu, Z. Yang, J. Li, X. Chen, X. Li and J. Sun, A novel orange–red emitting phosphor Sr_2LuTaO_6:Sm^{3+} for WLEDs, *J. Mater. Sci.: Mater. Electron.*, 2019, **30**, 9303–9310, DOI: 10.1007/s10854-019-01260-w.

125 A. Mondal and J. Manam, Structural, optical and temperature dependent photoluminescence properties of Cr^{3+}-activated $LaGaO_3$ persistent phosphor for optical thermometry, *Ceram. Int.*, 2020, **46**, 23972–23984, DOI: 10.1016/j.ceramint.2020.06.174.

126 D. Wu, L. Liu, H. Liang, H. Duan, W. Nie, J. Wang, J. Peng and X. Ye, $LiBAlF_6$:Cr^{3+} (B = Ca, Sr) fluoride phosphors with ultra-broad near-infrared emission for NIR pc-LEDs, *Ceram. Int.*, 2022, **48**, 387–396, DOI: 10.1016/j.ceramint.2021.09.114.

127 Y. Yang, Z. Lu, H. Fan, M. Chen, L. Shen, X. Zhang, Q. Pang, J. Chen, P. Chen and L. Zhou, Ultra-Broadband Near-Infrared Phosphors Realized by the Heterovalent Substitution Strategy, *Inorg. Chem.*, 2023, **62**, 3601–3608, DOI: 10.1021/acs.inorgchem.2c04347.

128 M. Zhao, Y. Liu, S. Ma, D. Liu and K. Wang, Investigation of energy transfer mechanism and luminescence properties in Eu^{3+} and Sm^{3+} co-doped $ZnWO_4$ phosphors, *J. Lumin.*, 2018, **202**, 57–64, DOI: 10.1016/j.jlumin.2018.05.030.

129 A. K. Bedyal, A. K. Kunti, V. Kumar and H. C. Swart, Effects of cationic substitution on the luminescence behavior of Dy^{3+} doped orthophosphate phosphor, *J. Alloys Compd.*, 2019, **806**, 1127–1137, DOI: 10.1016/j.jallcom.2019.07.305.

130 A. R. Beck, S. Das and J. Manam, Temperature dependent photoluminescence of Dy^{3+} doped $LiCaBO_3$ phosphor, *J. Mater. Sci.: Mater. Electron.*, 2017, **28**, 17168–17176, DOI: 10.1007/s10854-017-7645-4.

131 A. Douzi, S. Slimi, E. Madirov, A. Turshatov, B. S. Richards, R. M. Solé, M. Aguiló, F. Díaz, E. Ben Salem and X. Mateos, Structure and luminescence properties of Dy^{3+} doped quaternary tungstate $Li_3Ba_2Gd_3(WO_4)_8$ for application in wLEDs, *RSC Adv.*, 2023, **13**, 23772–23787, DOI: 10.1039/d3ra02501b.

132 Y. Xiang, Y. Zheng, L. Yang, M. Li, Y. Mao and J. Zhu, Exploring a new Dy^{3+}-activated borotellurate phosphor with thermally stable photoluminescence, *J. Alloys Compd.*, 2022, **919**, 165837, DOI: 10.1016/j.jallcom.2022.165837.

133 H. Zhong, X. Li, R. Shen, J. Zhang, J. Sun, H. Zhong, L. Cheng, Y. Tian and B. Chen, Spectral and thermal properties of Dy^{3+}-doped $NaGdTiO_4$ phosphors, *J. Alloys Compd.*, 2012, **517**, 170–175, DOI: 10.1016/j.jallcom.2011.12.072.

134 M. Behera, R. Panda, R. Arun Kumar, N. K. Mishra, K. Kumar and T. Del Monte, Microwave-assisted combustion synthesis and characterization studies of novel dysprosium doped yttrium calcium borate (Dy^{3+}:$Y_2CaB_{10}O_{19}$) phosphor materials for efficient white light applications, *Ceram. Int.*, 2024, **50**, 18146–18156, DOI: 10.1016/j.ceramint.2024.02.298.

135 F. Gao, W. U. Khan, W. U. Khan, Z. Ye and Y. Zhang, Structural-suppressing concentration quenching in dysprosium single-phase white emission and their application in optical thermometric and white light-emitting devices, *Ceram. Int.*, 2023, **49**, 8039–8047, DOI: 10.1016/j.ceramint.2022.10.322.